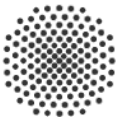

University of Stuttgart
Institute of Nano and Microelectronic Systems

ims chips

Master Thesis

Build up and characterization of an optical system with ultra-thin curved image sensors in foil

Kevin Carlos P

Examiner:	Prof. Dr.-Ing. Joachim N. Burghartz
Institute:	Institut für Nano- und Mikroelektronische Systeme (INES)
Supervisors:	M. Sc. Shuo Wang (IMS CHIPS) Dipl.-Ing. Markus Strobel (IMS CHIPS)
Start:	09.01.2023
Submission:	06.07.2023

Abstract

This thesis focuses on the construction of an optical system with ultra-thin bendable image sensors in foil, with an emphasis on evaluating image sharpness and investigating changes during bending of the imager embedded in a foil. The use of such curved image sensors in optical systems has the potential to greatly improve and overcome disturbing lens aberrations as well as to use lens complex optics. This thesis also involved a comprehensive literature review of curved image sensors, which provided insights into the potential advantages and challenges associated with their use. A hardware and software solution for reading out image data from the Chip Film Patch (CFP), a special technique to embed thin image sensors in a foil was also developed, along with data analysis techniques. Optical simulations and ray tracing were conducted to determine the optimal design for the optical system. This involved evaluating different beam paths and curvature configurations to achieve the best possible image quality. The optical design and construction process included the evaluation of image sharpness as a function of curvature.

The results of this study provide valuable insights into the design and construction of optical systems using ultra-thin curved image sensors. The findings demonstrate that the use of curved image sensors can greatly improve image quality, particularly at the edges of the image.

Overall, this thesis contributes to the field of optics and sensor technology by providing a comprehensive evaluation of the use of curved image sensors in optical systems. The findings of this study can improve the development of imaging technologies for a wide range of applications, including medical imaging and surveillance.

Acknowledgement

I would like to express my deepest gratitude and appreciation to all those who have contributed to the completion of this thesis. First and foremost, I am immensely grateful to my supervisors, Mr. Markus Strobel and Mr. Shuo Wang, for their guidance, expertise, and unwavering support throughout this research journey. Their insightful feedback, valuable suggestions, and continuous encouragement have been instrumental in shaping this thesis and enhancing my academic growth.

I am also thankful to Prof. Dr.-Ing. J. Burghartz for giving me the opportunity to work on this topic at IMS CHIPS and the staff members of IMS CHIPS for providing me with an enriching academic environment and the necessary resources to conduct my research. Their dedication to fostering intellectual curiosity has been inspiring. My sincere thanks also go to Ms. Lena Schad, for their time and valuable input by 3D printing of lens holders. Mr. Markus Schneider for making adapter boards for the image sensor foils. Their expertise and diverse perspectives have significantly contributed to the refinement of this study.

I am deeply indebted to my family and friends for their unwavering support and encouragement throughout this challenging endeavor. Their belief in my abilities, words of encouragement, and patience have been invaluable in keeping me motivated and focused.

In conclusion, the completion of this thesis would not have been possible without the collective efforts, support, and encouragement of all those mentioned above. I am truly grateful for their contributions and the impact they have had on my academic journey.

Table of Contents

List of Figures

List of Tables

List of Acronyms and Symbols

BCB Benzocyclobutene

CFP Chip Film Patch

CLC Circle of least confusion

HDRC High Dynamic Range CMOS

HySiF Hybrid System in Foil

PCB Printed Circuit Board

ROI Region of interest

d Diameter of lens aperture

F# F-number of a lens

f Focal length

FF Field Fraction

m Magnification

R Radius of Curvature

$\mathbf{r_0}$ Radius of polar coordinates of cylindrical object

Y Object height

Y' Image height

Z Object distance

Z' Image Distance

$\boldsymbol{\omega}$	Object and image angle
$\boldsymbol{\alpha}$	Angle of polar coordinates of cylindrical object
$\boldsymbol{\Delta Z'}$	Defocus of the image plane relative to the ideal (paraxial) image plane
$\mathbf{Z}_0$	Distance from the center of the object to the center of the lens on the optical axis

1 Introduction

Curved image sensors are a cutting-edge technology that has the potential to completely change the field of imaging by enabling higher image quality and more compact designs. These sensors are designed to conform to curved surfaces, which allows them to capture light more efficiently and with greater precision than traditional flat sensors.
These image sensors have the ability to minimize or even completely eliminate certain optical imperfections of lenses that can impair image quality. These lens aberrations include spherical aberration, astigmatism, coma, curvature of the image plane and distortion, which can be significantly reduced by utilizing a curved sensor thereby increasing image sharpness.
Curved image sensors also reduce the size and bulk of cameras in addition to enhancing image quality. This is due to the fact that the sensor's curved shape enables a more streamlined design, requiring fewer optics to correct for aberrations. Despite many advantages of curved image sensors like reduced aberrations and improved image quality, there are a few challenges associated with fabricating and integrating curved image sensors such as the need for specialized manufacturing processes and the potential for increased costs [1]. There are recent advances in curved sensor technology, including the development of sensors with extreme curvatures and the incorporation of flexible substrates to enable conformal sensors [1]. Curved image sensors can be highly helpful in a variety of applications, including consumer electronics, security, and medical imaging.
This thesis presents the study of the curved image sensors with relevant optical simulation and ray tracing, determining the hardware and software solution for reading out the image data from the Chip Film Patch and finally design and construction of the optical setup with a single lens and an adjustable cylindrical bending of the imager foil. The bending is used to exhibit optimum sharpness across all the pixel area and not

only in the center of the sensor.
This thesis is organized into five chapters, including this introduction. Chapter two gives a historical perspective on curved image sensors and gives a general overview on Chip film Patch (CFP) and the system in foil. This chapter also discusses different approaches of manufacturing of the CFP and also discusses hybrid system in foil. Chapter three discusses the optical simulation giving a general overview on the WinLens software, different types of lenses and the simulation to correct the image sharpness as well as calculation of the radius of curvature. Chapter four describes the optical setup and reading the image from the CFP while verifying if the radius of curvature is similar to the theoretical value calculated during the simulation. Finally, in Chapter five, conclusion and an outlook of the future work is presented.

2 Overview of curved image sensors

2.1 History of curved image sensors

Although the idea of curved image sensors has been studied for many years, it is only recently that the technology has developed to the point where it is being considered for real-world applications. This section provides a comprehensive history of curved image sensors, covering significant academic works and scientific developments that have contributed to the current state of the art.

The earliest research on curved sensors dates back to the 1980s, when researchers investigated the use of curved detectors for X-ray imaging. Their findings indicated that a curved detector could reduce the amount of scattered radiation that reached the detector, resulting in clearer and more accurate images. However, the technology was not widely adopted due to the complexity and cost of fabricating curved sensors at the time [2].

In the early 2000s, researchers proposed the concept of using curved sensors in digital cameras to reduce optical aberrations [2]. They found that a curved sensor could reduce distortion and other aberrations by allowing for more precise focusing of light onto the sensor surface. However, the technology was not feasible at that time due to limitations in the manufacturing process and the difficulty of integrating curved sensors into camera designs.

In 2012, Sony made an announcement regarding the development of a curved CMOS image sensor with a radius of curvature of 5 mm. The sensor was designed to reduce distortion and improve low-light perfor-

mance. Nevertheless, the sensor was not widely adopted due to production constraints and difficulties in integration into existing camera modules.

In 2017, a team of researchers announced the development of a flexible curved image sensor. The sensor was made from a thin layer of silicon mounted on a flexible substrate, allowing it to conform to a various curved surfaces. Compared to traditional flat sensors, the sensor demonstrated improved light sensitivity and reduced distortion.

Another breakthrough occurred in 2019, when researchers developed a curved sensor with a radius of curvature of 3.5 mm. The sensor demonstrated improved image quality and reduced optical aberrations compared to flat sensors [1].

In 2020, further progress was made with the announcement of a curved CMOS sensor with a radius of curvature of 50 mm. The sensor was designed for panoramic imaging applications and image quality improvement [3].

These recent breakthroughs have led to increased interest in curved sensors for various applications, including medical imaging, automotive cameras, and security cameras. The development of flexible substrates and advanced manufacturing processes has enabled the fabrication of sensors with extreme curvatures, opening up new possibilities for sensor design and integration.

In conclusion, the history of curved image sensors is one of gradual development and improvement over several decades. Recent advancements in sensor design and fabrication have led to the development of sensors systems with enhanced image quality and reduced optical aberrations. As the technology continues to evolve, we can expect to see even more advanced and innovations of curved sensors in a wide range of imaging applications.

2.2 Applications and advantages of using bendable image sensors

Bendable image sensors, also known as flexible image sensors, are emerging technologies that offer unique advantages and open up new possibilities for various applications. These sensors can be bent or curved without compromising their performance, making them suitable for applications where traditional rigid sensors would be limited.

One of the key advantages of bendable image sensors is their ability to withstand bending or curving without breaking, which increases their durability compared to traditional rigid sensors. This flexibility enables seamless integration into various form factors, making them suitable for applications that require conformal or curved surfaces.

The ability of these sensors to capture images in unconventional shapes or angles provides enhanced sensing capabilities. They can conform to irregular surfaces, allowing for imaging in tight spaces or non-planar objects. This feature enables new imaging applications in fields such as medical diagnostics, robotics, and industrial inspection.

Another advantage of bendable image sensors is their lightweight nature which makes them ideal for portable devices and wearable technologies. By reducing weight and size, these sensors enable the development of compact imaging systems, such as lightweight cameras and augmented reality (AR) glasses, without compromising image quality. They can be integrated into a wide range of materials and substrates, including curved surfaces, plastics, and even fabrics. This versatility unlocks possibilities for integrating imaging capabilities into everyday objects, such as smart clothing, flexible displays, automotive interiors, and Internet of Things (IoT) devices.

Bendable image sensors find significant applications in the medical field. Their ability to conform to curved surfaces allows for advanced imaging techniques, including endoscopy and minimally invasive surgeries [4]. Additionally, bendable sensors integrated into wearable devices can monitor vital signs and provide real-time healthcare monitoring [5].

The integration of bendable image sensors into consumer electronics has opened up new possibilities for innovative products. Foldable smartphones and wearable cameras are some examples [6]. These sensors enable seamless user experiences by providing high-quality imaging and display capabilities on bendable and curved surfaces [7].

2.3 Manufacturing techniques of curved image sensors

2.3.1 Hybrid System in Foil (HySiF)

Hybrid systems in foil, also known as hybrid electronics, represent a relatively new technology that combines the benefits of both traditional printed circuit board (PCB) technology and flexible electronics. Hybrid systems in foil are fabricated by integrating rigid and flexible materials into a thin, flexible substrate, resulting in lightweight and high performance electronic devices that can be used in a wide range of applications [8].

One of the main advantages of hybrid systems in foil is their versatility, allowing for a wide range of applications such as medical devices, consumer electronics, and automotive applications. For example, they can be utilized to create flexible sensors that can be worn on the skin to monitor vital signs, or to create lightweight displays for automobile applications [9].

Durability is another advantage of hybrid systems in foil. Unlike traditional PCBs, which are rigid and can break easily, hybrid systems in foil are flexible and can withstand greater degrees of bending and twisting without breaking. This makes them well suited for wearable technology and other applications where flexibility and durability are important.

The fabrication of hybrid systems in foil involves the integration of both rigid and flexible materials. The rigid materials typically consist of conventional PCB materials like copper and fiberglass, while the flexi-

ble materials are made from materials like polyimide or other plastics. These materials are then integrated into a thin, flexible substrate, such as a polymer film, to create a hybrid system in foil.

One of the main challenges associated with hybrid systems in foil is the integration of different materials. Because these systems incorporate a mixture of rigid and flexible materials, there can be issues with compatibility and reliability. However, researchers are actively working to overcome these challenges by developing new materials and fabrication techniques [10]. A specific technique used in hybrid systems in foil is Chip Film Patch (CFP), which will be discussed in detail in the next section.

In conclusion, hybrid systems in foil are a promising technology that merges the advantages of traditional PCB technology with the flexibility and durability of flexible electronics. They offer a versatile, lightweight, and high-performance alternative to traditional electronic devices, and are ideal for use in a wide range of applications. While there are still some challenges to overcome, the potential benefits of hybrid systems in foil make them an area of active research and development [11].

2.3.2 Chip Film Patch (CFP) process flow and approaches

Chip Film Patch technology is a relatively new development in the field of electronics and engineering. It involves the fabrication of thin films that are capable of adhering to surfaces, and embedding electronic components like sensors and wireless communication modules. These thin films, known as patches, have various applications, including monitoring vital signs and tracking physical activity [12].

In 2011, the CFP was developed at the Institute for Microelectronic Stuttgart (IMS CHIPS). Two concepts are employed in CFP: face-up and face-down CFP. The labs at IMS CHIPS primarily use the face-up concept. One of the key advantages of CFP is its compatibility with IC processing lines, enabling fine-pitch connectivity (10 µm) and large I/O counts. Figure 2.1 depicts the CFP's process flow [13].

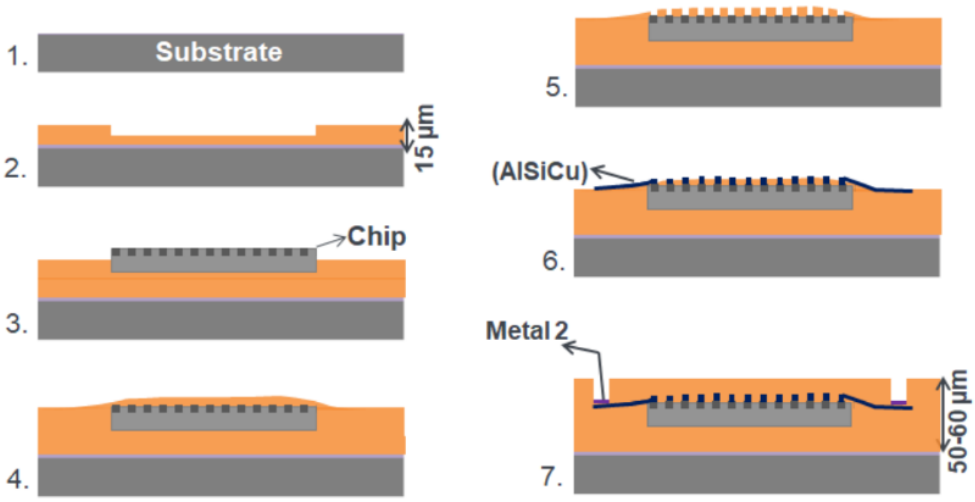

Figure 2.1: Schematic process flow of the CFP, 1) depositing adhesion lowering layer on silicon carrier, 2) polymer coating and cavity opening, 3) face-up chip embedding in cavity, 4) top polymer coating and surface planarization, 5) via opening, 6) metallization and metal patterning, 7) polymer coating, outer pad opening, further metallization, and releasing CFP from temporary carrier. Source: [13].

From Figure 2.1, The process of creating chip film patches starts with surface treatment. The subsequent steps involve coating polyimide and the creation of the cavities. A fine placer is then used to insert, ultra-thin image sensor chips into the previously created cavities, followed by spin coating of polyimide and BCB (benzocyclobutene) to cover the embedded chips. After opening of chip pads area, AlSiCu sputtering is performed onto the BCB layer and lithographically structured to connect the chips to outside pads on the foils. Finally, the pixel region of image sensors and outside pads are opened using plasma etching [14].
After the completion of the chip film patch fabrication process, the patch can be attached to a substrate with a variety of materials, including paper, metal or fabric. The attachment is typically done using an adhesive, allowing the chip film patch to be securely affixed to the desired surface, such as the skin when used for medical or wearable applications [15]. In this research, the patch was attached to a bendable metal sheet, which will be further explained in Chapter 4.

2.4 CFP Imager Foil and Lens Specifications

2.4.1 Embedded image sensor specification

The image sensor foil used in this thesis is shown in the Figure 2.3. This sensor foil was used for the bending tests as well as in the optical setup developed in this thesis and to evaluate the Radius of curvature. The relevant specifications of the High Dynamic Range CMOS (HDRC) image sensor for optical design and simulation are shown in the Table 2.1. These data were obtained from the HDRC- VGA4 data sheet [16] provided by IMS CHIPS.

Table 2.1: Specifications of the image sensor used [16].

Image sensor HDRC-VGA4	**Values**
Pixel size	4.6 µm
Resolution Full	768 x 496 pixel
Resolution Region of Interest (ROI)	640 x 480 pixel
Pixel area Full	3.53 x 2.28 mm
Pixel area ROI	2.94 x 2.21 mm

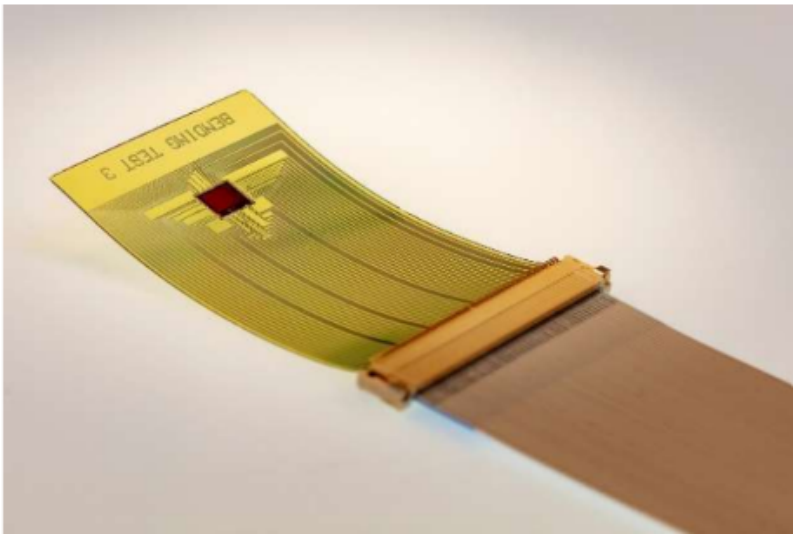

Figure 2.2: A CFP patch with the embedded HDRC VGA4 image sensor. Source: [14]

2.4.2 Lens specifications

A goal of this thesis is to use an inexpensive and low complex optics with high light throughput (low f-number). To improve the image formation by minimizing lens aberrations and increasing image sharpness the additional degree of freedom of bending the image sensor is to be evaluated. Various lenses were used and tested in this thesis. After considering the image sensor and system specifications and the available lenses in WinLens and commercially available, a lens with a focal length of 7.5 mm and a F# of 1.5 was chosen for the optical system. The f-number is a measure of an optical system's capacity to gather light and is calculated by dividing focal length f by the diameter of the aperture d. In this case, the diameter of the aperture used in the optical system is 4.7 mm which is specified in Figure E.4 in the appendix for the 3D-printable lens holder design and aperture specification. The lens specifications are shown in Table 2.2, which provides details on the characteristics of the used and available lens at IMS CHIPS in the study.

Table 2.2: Lens Specifications of finally chosen lenses in IMS CHIPS.

Lens Specs	**Values**
Lens Type	Achromat
Diameter	5 mm
Focal Length	7.5 mm
F#	1.5
F# with d= 4.7 mm	1.6

Figure 2.3: 7.5 mm Achromat Lens available at IMS CHIPS. Source: [17].

2.5 Summary

"Chip film patch" and "Hybrid system in foil" are two distinct technologies used in the field of electronics. A chip film patch refers to a miniaturized circuits or a sensor mounted on a flexible film substrate. It offers advantages such as compact size, lightweight, and flexibility, making it suitable for applications like wearable devices and medical sensors. On the other hand, a hybrid system in foil combines different electronic components, including ICs, passive elements, and sensors, into a single flexible foil-based system. This technology enables complex functionalities in a compact and flexible form factor, commonly used in applications like smart cards and flexible circuits.

3 Optical simulation

3.1 Introduction to the WinLens software

WinLens is a powerful optical design software that is widely used in the field of optics and lens design. It provides a comprehensive set of tools and features for designing, analysing, and optimizing optical systems. With its user-friendly interface and robust capabilities, WinLens has become a popular choice among professionals and researchers working in various industries, including aerospace, defence, telecommunications, and photography.

Optical design involves the creation and optimization of lens systems to control the behavior of light. This includes designing lenses for imaging systems, such as cameras and telescopes, as well as for non-imaging applications, such as laser systems, fiber optics, and illumination systems. The goal is to achieve specific performance criteria, such as image quality, field of view, resolution, and aberration correction.

WinLens simplifies the complex process of optical design by providing a graphical user interface that allows users to easily define and manipulate lens elements, light sources, detectors, and other optical components. It offers a range of design tools, such as ray tracing, optimization algorithms, and analysis modules, to assist users in creating and evaluating optical systems.

One of the key features of WinLens is its ability to perform accurate ray tracing simulations. Ray tracing is a fundamental technique used in optical design to determine the path of light rays through an optical system. WinLens utilizes advanced algorithms to trace rays through complex lens systems, taking into account factors such as refraction, reflection, diffraction, and scattering. This allows designers to visualize

and analyze the performance of their optical systems, identify potential issues, and make informed design decisions.

3.1.1 WinLens Features and Functionalities

WinLens offers a comprehensive set of features and functionalities that facilitate the design and analysis of optical systems. Some of the key features of WinLens include [18]:

Lens Design: WinLens provides a range of tools for designing lenses, allowing users to specify lens parameters such as focal length, aperture, and surface curvatures. It supports the design of both spherical and aspheric lenses, enabling the creation of complex lens systems.

Optical Components: The software offers a library of optical components, including lenses, mirrors, prisms, filters, and diffractive elements. Users can select and configure these components to build their optical systems easily.

Ray Tracing: WinLens employs advanced ray tracing algorithms to simulate the propagation of light through the designed optical system. This enables users to analyze various optical properties, such as image formation, aberrations, and beam profiles.

Optimization: The software provides optimization algorithms that allow users to optimize the performance of their optical systems. By specifying optimization goals and constraints, users can automatically adjust system parameters to achieve desired outcomes, such as minimizing aberrations or maximizing image quality.

Tolerance Analysis: WinLens offers tools for tolerance analysis, allowing users to evaluate the impact of manufacturing and assembly errors on the performance of the optical system. This helps to ensure that the designed system is robust and capable of meeting performance specifications in real-world conditions.

The importance of optical design software in the field of optics and photonics cannot be overstated. It accelerates the design process, improves system performance, and reduces development costs.

3.1.2 Coordinate System in WinLens

A clearly defined coordinate system is essential for accurately modelling and manipulating optical components and their interactions within an optical system in optical design software like WinLens. The coordinate system acts as a foundation for determining the locations, directions, and sizes of optical components as well as for evaluating their functionality. We will examine the WinLens coordinate system and its importance in optical design in this section. In this thesis this coordinate system is used and all values like object/image distance and object/image height are related to it.

To specify the locations and orientations of optical components inside an optical system, WinLens uses a Cartesian coordinate system. Three axes X, Y, and Z that are mutually perpendicular make up the Cartesian coordinate system. The optical axis, or direction of light propagation, is represented by the Z-axis. The X-axis indicates the horizontal direction, the Y-axis represents the vertical direction, see Figure 3.1.

The principal or chief ray of an object point and the optical axis intersect at the coordinate system's origin where the lens is positioned as shown in Figure 3.2.

As we can see in the Figure 3.2, the projection by a round lens has a rotational symmetry, therefore only the Z and Y axis is sufficient for ray simulations as shown in Figure 3.3. The object distances have a negative Z value and Image distances have positive Z values, according to coordinate system of WinLens.

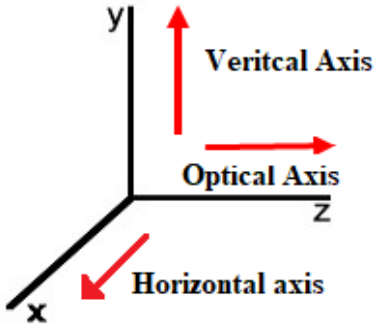

Figure 3.1: Cartesian Coordinate system of WinLens [19].

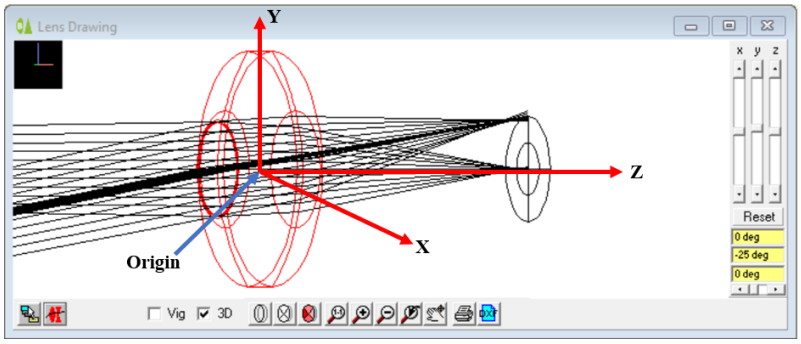

Figure 3.2: Coordinate system with lens and simulated ray fans of two object/image points (3D).

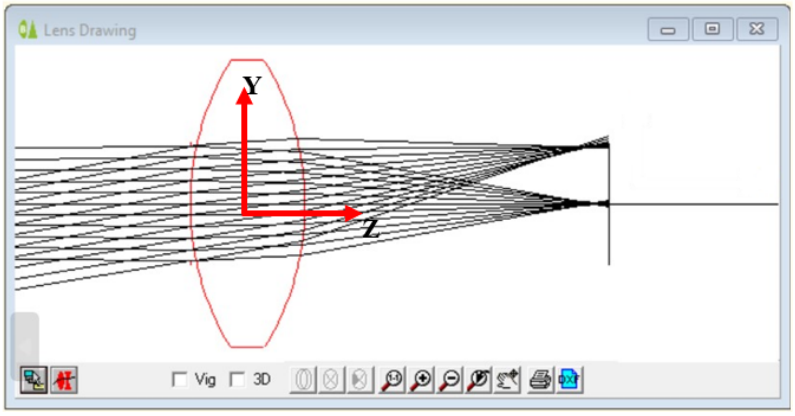

Figure 3.3: Coordinate system used in simulation showing the Y/Z cross section of the ray fans (2D).

In WinLens, coordinate transformations are used to specify the location and orientation of optical components. The component coordinate system, which corresponds to each optical component, is its own unique

local coordinate system. In relation to the optical system's global coordinate system, the component coordinate system is specified. The coordinates of an optical component (X, Y, and Z) in the global coordinate system are used to position it. These coordinates specify where a reference point on the part, like the center of a mirror or the vertex of a lens, is located. The component can be positioned precisely within the optical system by providing the X, Y, and Z coordinates.

Once the optical components are positioned and oriented within the global coordinate system, WinLens enables the analysis of the optical system's performance. This analysis includes ray tracing simulations, wavefront aberration calculations, and optimization of system parameters.
Ray tracing involves tracing individual rays of light from an object point through the optical system to the image plane to determine the paths, intersections, and interactions of the rays with the optical components. The coordinate system is crucial in accurately calculating the ray paths and analyzing properties such as image formation, spot diagrams, and aberrations.

3.1.3 Types of Lenses in WinLens

In this section we look at common types of lenses in WinLens along with a brief comparison:

Spherical lenses have curved surfaces, and their shape can be described by a single radius of curvature. They are the most basic and widely used type of lenses. Spherical lenses suffer from spherical aberration, which causes different wavelengths of light to focus at different points, resulting in blurring of the image. These lenses are examined later in the section.

Aspheric lenses have non-spherical surfaces that help to correct aberrations and improve image quality. These lenses are designed with complex surface profiles to reduce spherical aberration and other optical imperfections. Aspheric lenses are commonly used in high-performance optical systems where image quality is crucial.

Achromatic lenses are made to reduce chromatic aberration, which is

brought on by the dispersion of light. They are made up of numerous lens components produced from various glass kinds with various dispersion characteristics. The combination of these components aids in bringing various light wavelengths to a single point of focus, which enhances colour correction. These lenses were considered in this thesis as image sharpness was better and are explained in detail in the later stage of the chapter.

Apochromatic lenses are advanced versions of achromatic lenses that provide even better color correction. They are designed to reduce not only chromatic aberration but also other aberrations like spherical aberration and coma. Apochromatic lenses typically use more lens elements made from specialized glasses to achieve superior image quality.

Telephoto lenses are used to magnify distant objects and are commonly used in photography and surveillance applications. These lenses have a longer focal length than their physical length, achieved through a combination of lens elements and a telephoto group. Telephoto lenses allow for a narrow field of view and a shallow depth of field.

Zoom lenses offer variable focal lengths, allowing the user to change the magnification of the lens without physically changing it. These lenses use a combination of lens elements that can be adjusted to change the focal length. Zoom lenses provide flexibility in capturing images at different magnifications, but they tend to be more complex and bulkier than fixed focal length lenses.

When comparing these lenses, factors to consider include image quality, aberration correction, focal length range, ease of use, size, weight, and cost. The optimal choice of lens depends on the specific application and requirements of the optical system. WinLens provides tools to analyze and optimize the performance of these lenses based on the user's design parameters.

3.2 Optical Aberrations

Optical aberrations are inherent deviations from ideal optical performance that can occur in imaging systems, such as cameras, telescopes, and microscopes. These aberrations introduce various distortions and degrade image quality. Understanding the nature of optical aberrations and developing effective correction methods are crucial for achieving high-quality imaging results in a wide range of applications. Now, we will delve into different types of optical aberrations, their causes as well as in aberration correction techniques.

3.2.1 Types of optical aberrations

Chromatic aberration arises from the dispersion of light, causing different wavelengths to focus at different distances from a lens or mirror. Figure 3.4 shows the effect of longitudinal chromatic aberration for rays with different wavelengths parallel to the optical axis. This results in color fringing and reduced image sharpness. In Figure 3.5 the resulting Lateral chromatic aberrations for skewed rays is shown resulting in different image sizes for red and blue colour. To mitigate chromatic aberration, various techniques have been employed. These include the use of low-dispersion glass elements or diffractive optical elements in lens design, as well as the development of apochromatic lenses with enhanced colour correction capabilities [20]. Achromat lenses correct chromatic aberration and is explained in the later stages of the chapter.

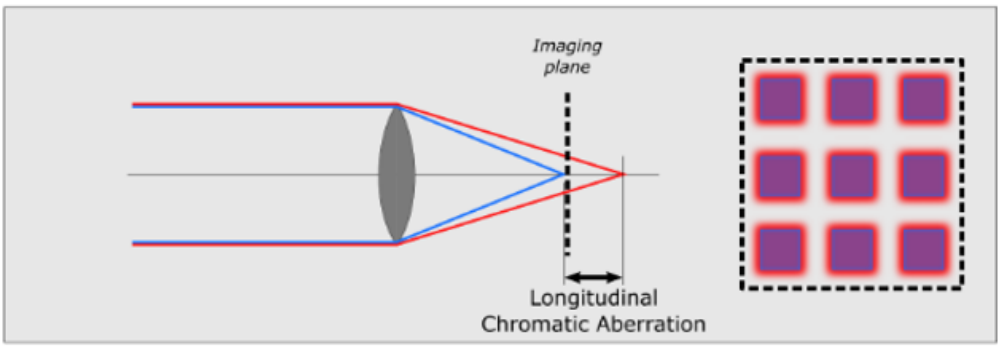

Figure 3.4: Longitudinal Chromatic Aberration. Source: [21].

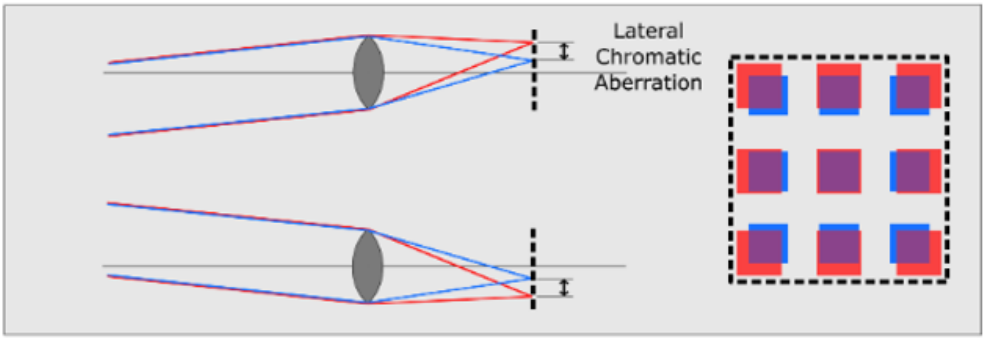

Figure 3.5: Lateral Chromatic Aberration for different distances from the optical axis. Source: [21].

Spherical aberration occurs due to the differences in focal points for parallel light rays passing through different portions of a spherical lens. It leads to blurred images and limits the achievable resolution. Aspherical lenses or specialized corrective elements, such as phase plates, have been introduced to compensate for spherical aberration and improve image quality. Additionally, the advancement of computer-aided design and manufacturing techniques has facilitated the production of more precise aspheric surfaces [22]. As we can see in the Figure 3.6 for an ideal lens, rays are focused at a single point and there is no spherical aberration whereas in the real lens shown in Figure 3.7 there is spherical aberration as parallel rays are focused at different points. On the image plane this results in a blurred spot as you can see in the spot diagram in Figure 3.7 right. There is a focal plane where the blurred spot has a minimum, this is the **Circle of Least Confusion (CLC)**.

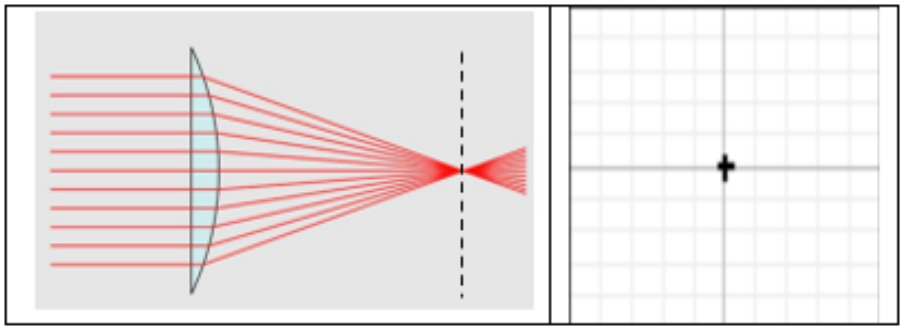

Figure 3.6: Ideal lens with no spherical aberration and its spot diagram. Source: [23].

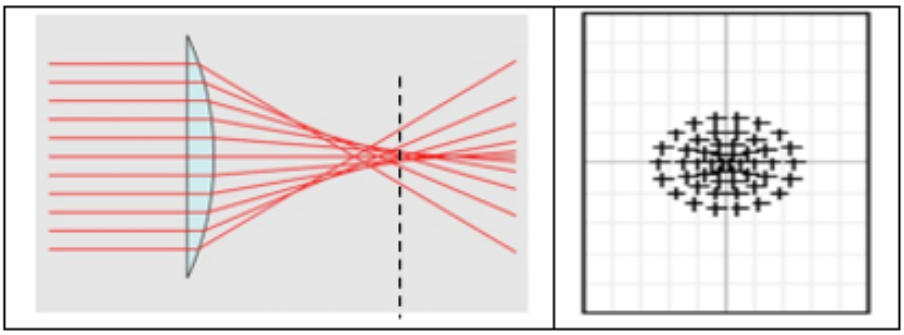

Figure 3.7: Spherical aberration in a real lens and its spot diagram. Source: [23].

Coma is an aberration that causes off-axis points to appear as comet-like shapes in images, resulting in a loss of sharpness and detail, see Figure 3.8. Coma occurs when off-axis rays focus at different points due to the non-rotationally symmetric incident to the optical elements. To minimize coma, optical designs incorporating multiple lens elements or utilizing aspheric surfaces have been employed. Additionally, advancements in computational imaging techniques, such as wavefront coding, have shown promise in correcting coma aberration [24].

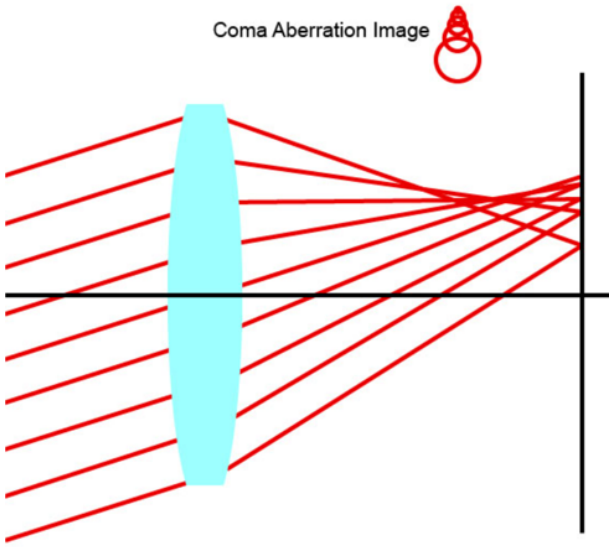

Figure 3.8: Coma Aberration. Source: [25].

Astigmatism is an optical aberration that affects the focusing ability of an optical system, resulting in distorted or elongated images. It occurs when the curvature of the lens or cornea is uneven in different meridians. In the case of the human eye, astigmatism can lead to blurred vision, where objects appear stretched or distorted. The effect of astigmatism is visually represented by point sources appearing as elongated or blurred lines instead of sharp points. Figure 3.9 depicts two distinct focal points of rays belonging either to the tangential plane (also name meridional plane) or the sagittal plane perpendicular to the tangential. This aberration can be corrected using corrective lenses with cylindrical surfaces that have different curvatures in different meridians. Toric lenses, which have different powers in different orientations, are commonly used to compensate for astigmatism and provide clear and focused vision. In recent years, innovative approaches, such as liquid crystal adaptive optics, have been explored to dynamically correct astigmatism aberration in real-time[26].

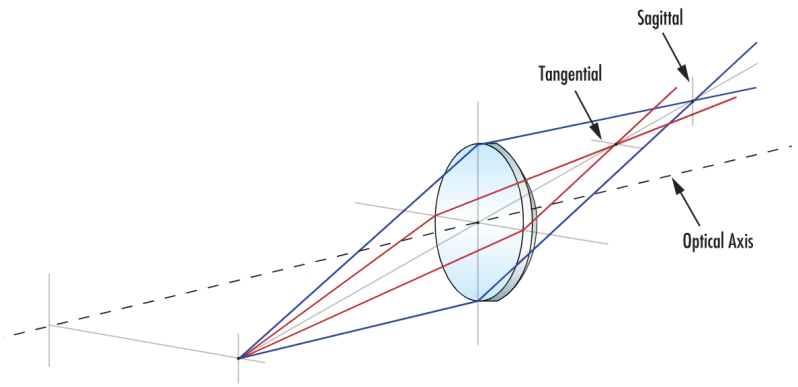

Figure 3.9: Astigmatism. Source: [27].

Astigmatism can have a significant impact on various optical systems, including cameras, microscopes, and telescopes. It is crucial to correct astigmatism to achieve accurate imaging and precise measurements. Advancements in lens design and manufacturing techniques have enabled the production of highly precise toric lenses, allowing for effective correction of astigmatism. By addressing astigmatism, optical systems can deliver improved image quality, sharper details, and enhanced visual perception in both medical and technological applications.

Petzval Field curvature describes the aberration in which a flat object is not projected into a flat image plane but instead is focused on a curved surface called the Petzval surface, see Figure 3.10. Astigmatism is closely linked to the field curvature, since there is mathematical relation between the curved Petzval surface and curvatures of tangential and sagittal surfaces of the astigmatism aberration. Field curvature can be corrected by an additional field flattener lens [28]. In this thesis, we mainly concentrate on improving the astigmatism as the image quality is affected more by astigmatism than any other aberration.

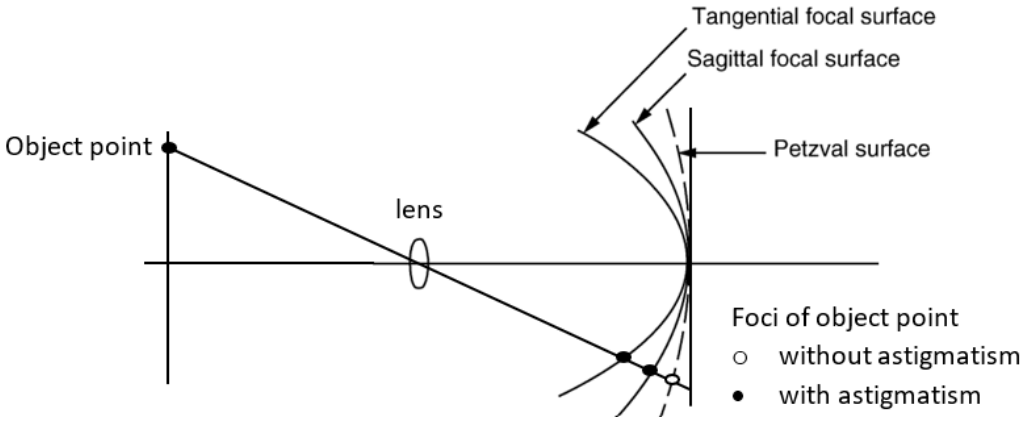

Figure 3.10: Field curvature plot amended according to [28] and [29].

Geometric Distortion refers to the non-linear mapping of object points onto the image plane, causing image warping. Common types of distortion include barrel distortion, where straight lines appear curved outward, and pincushion distortion, where lines appear curved inward. Figure 3.11 demonstrates the visual effect of barrel distortion, where the horizontal lines curve outward. Sophisticated lens designs, complex lens arrangements, or software-based correction algorithms are used to reduce or eliminate distortion artifacts [30]. Geometric distortion is not relevant in this thesis as it can be corrected by software algorithms in an image processing system.

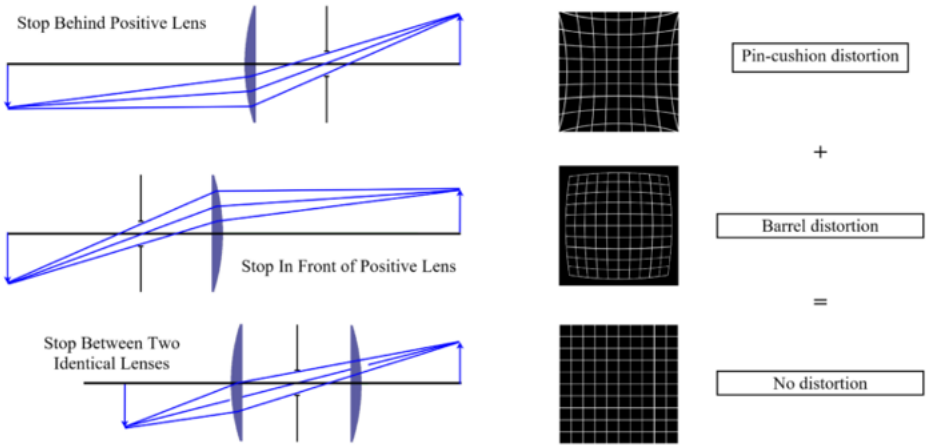

Figure 3.11: Distortion. Source: [31]

3.2.2 Consequences and restrictions on optical simulation and design

All before mentioned aberrations normally superimpose on the projected image and disturb the image formation process all together. For this thesis, with the goal to use a low complex and inexpensive optics with the additional degree of freedom by the bendable image sensor, some justified simplifications are being made to reduce the scope of the technical problem without sacrificing the design goal much:

- An achromatic lenslet was used instead of a single lens in order to omit the chromatic aberration and is shown in section 3.3.1. The optical simulations can therefore be done for the monochromatic case.

- Geometric distortion is not of interest since it is correctable with image processing algorithms after image acquisition.

- The coma aberration occurring at off-axis object points will be limited by choosing not wide-angle field of view with moderate object angles below 15° to the optical axis meaning a field of view below 30°.

– The highest remaining contributions for aberrations to be corrected and improved by the bendable image sensor in foil is the field curvature in conjunction with the astigmatism which is of most relevance in the optical simulation.

An additional advantage of a curved image sensor is, e.g., in an inspection system, that the object can be allowed to be strongly shaped instead of being mostly plane. This would allow to use a lens with a low f-number, which have a high capacity to gather light but suffer from low depth of focus in the object space. This will be studied in the thesis with cylindrical shaped objects like beverage cans.

3.3 Simulation Results

3.3.1 Simulation using different lenses

Simulation of spherical and aspherical lenses in WinLens, allows for accurate and comprehensive analysis of their optical properties. Spherical lenses like bi-convex lenses, also known as convex-convex lenses, are widely used in various optical systems for their ability to converge light rays and focus them to a specific point. Aspherical lenses are lenslets composed of two bonded single lenses to reduce the chromatic aberration to a high extent compared to spherical lenses.

With WinLens, we can create simulation for these lenses and explore their performance under different conditions. The software provides a user-friendly interface that facilitates the creation and manipulation of lens designs.

One of the key advantages of using WinLens for simulation is the ability to simulate the lens's behavior with different input parameters. We can vary factors such as the lens material, radius of curvature, focal length, object distance and image distances and many more to understand how these variables affect the lens's performance. This flexibility enables the optimization of lens designs for specific applications, such as imaging systems, telescopes, or microscopy.

WinLens also allows for the analysis of aberrations, which are optical imperfections that can degrade image quality. By incorporating aberration analysis tools, the software enables us to evaluate and minimize aberrations when using different types of lenses. This feature is crucial for achieving high-quality imaging and precise focusing in optical systems.
Additionally, we can see comprehensive visualization capabilities, allowing us to observe ray traces, spot diagrams and wavefront aberration. Spot diagrams in optical simulation are visual representations that show the point spread of light rays on an image plane, helping to evaluate the image quality and the effects of aberrations in an optical system. These visual representations help us understand the behavior of biconvex lenses, identify potential issues, and make informed design decisions.

From the below figures, we can see the simulation using a bi-convex lens of focal length f = 10 mm available in the lens catalog integrated in WinLens. The object is placed at distance at Z = -150 mm with a viewing angle of ±10°, defining the maximum one-sided field height of the object (Y) and the image (Y'). These values are in the range of the setup to be evaluated. From the Figure 3.12, we can see rays coming from two object points (from the left), one on-axis and one at maximum field height, being focused at two image points on the image plane (inside red circle).

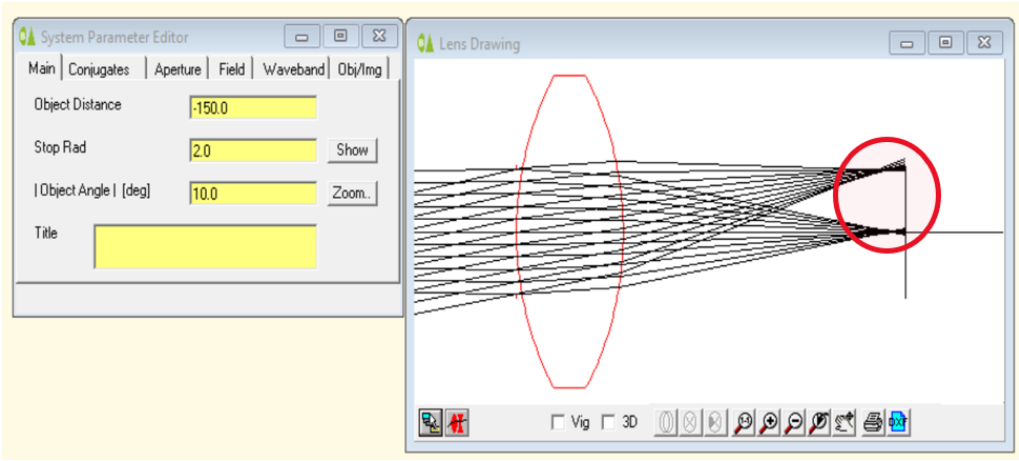

Figure 3.12: Simulation of bi-convex lens for a focal length of 10 mm.

The full field spot diagrams for this simulation of the biconvex lens in Figure 3.13, shows spot patterns over one quarter of the image plane with four distinct image positions (on-axis, bottom, right, diagonal) for the monochromatic case. We can see that the points of light rays are spread around a center at the defocus values of $\Delta Z' = 0$ mm from the image plane. Figure 3.14 shows the even increased diameters of the spot diagrams for the chromatic case with 5 wavelengths.

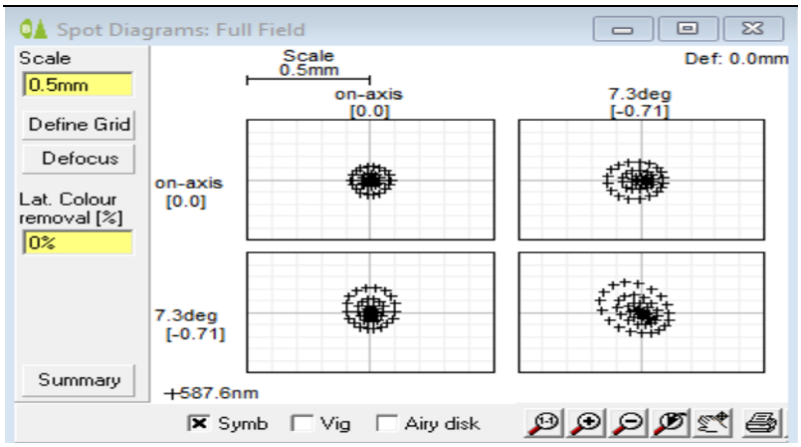

Figure 3.13: Spot diagrams of bi-convex lens for a focal length of 10 mm.

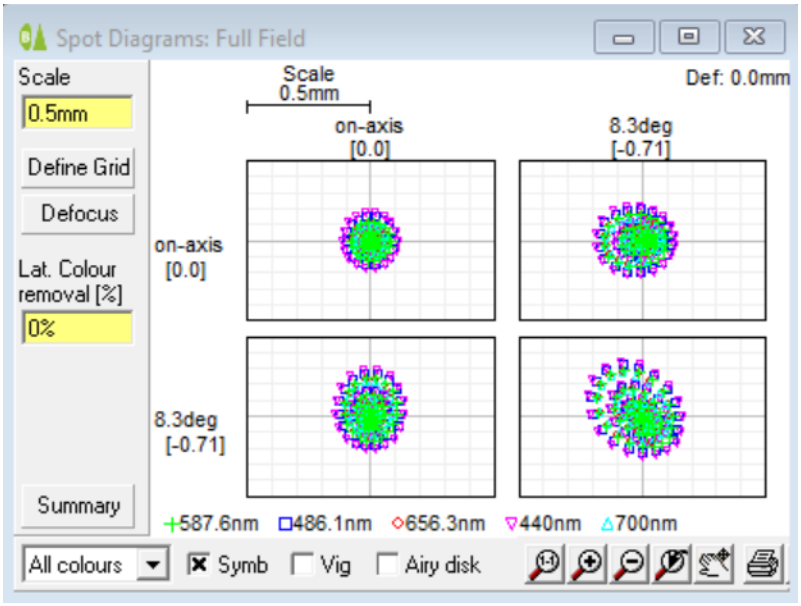

Figure 3.14: Spot diagrams of bi-convex lens for a focal length of 10 mm with 5 different wavelengths.

In the left plot of the field aberrations graph Figure 3.15 we can see the sagittal (S-field) and tangential (T-field) components of the astigmatic aberration (introduced in Figure 3.9) including Petzval Field curvature (Figure 3.10). The plot shows the field curvatures referring to previous Figure 3.10. The horizontal axis gives the defocus value ΔZ' and the vertical axis the normalized Field Fraction $FF = Y'/Y'_{max}$.

Our goal is to compromise on both S- and T-fields and reduce the astigmatism aberration by bending of the image sensor. This is explained in the later stages of the chapter.

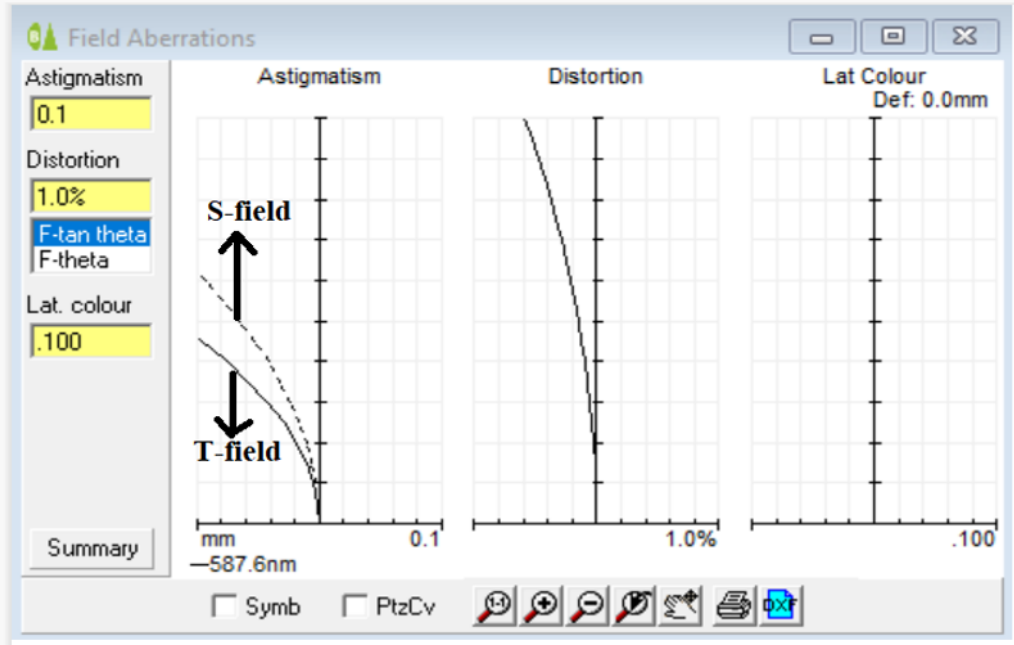

Figure 3.15: Field aberrations of bi-convex lens for a focal length of 10 mm.

Utilizing achromat lenses and simulating in WinLens provides a good approach to analyzing and designing optical systems compared to spherical lenses. Achromatic lenses, unlike biconvex lenses, are specifically designed to minimize chromatic aberrations by combining different types of glass with varying dispersions.
One of the advantages of using WinLens for achromat lens simulation is its ability to accurately predict and analyze chromatic aberrations. Chromatic aberrations occur when different wavelengths of light focus

at different points, resulting in color fringing and reduced image quality. Achromat lenses allows us to minimize these aberrations, resulting in sharper and more accurate imaging compared to biconvex lenses.
The following Figures represent simulations for an achromat lens for a focal length of 8 mm available in the building WinLens catalog as done before for the biconvex lens with same system parameter, spot diagrams and lens aberration analysis.

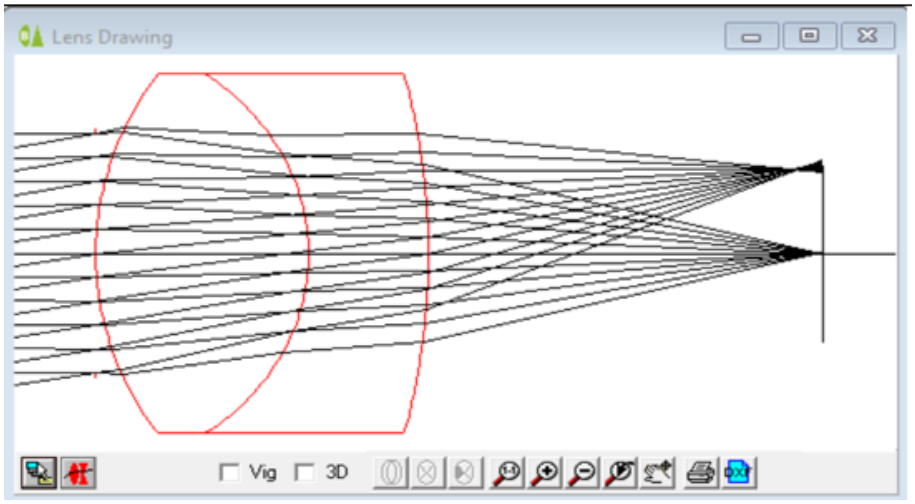

Figure 3.16: Simulation of achromat lens for a focal length of 8 mm.

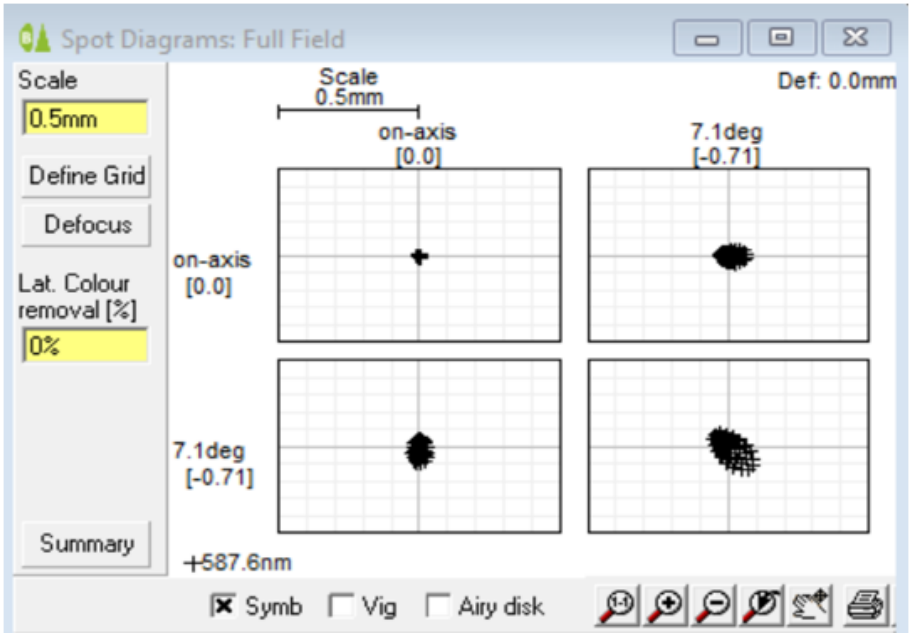

Figure 3.17: Spot diagrams of achromat lens for a focal length of 8 mm.

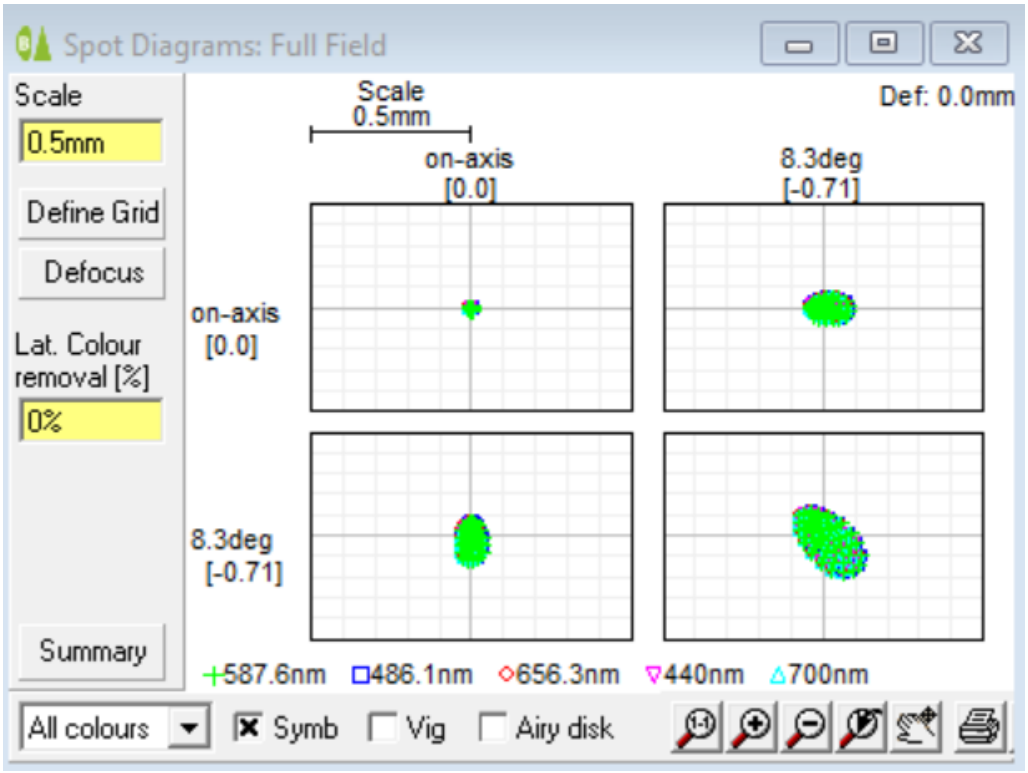

Figure 3.18: Spot diagrams of achromat lens for a focal length of 8 mm with 5 different wavelengths.

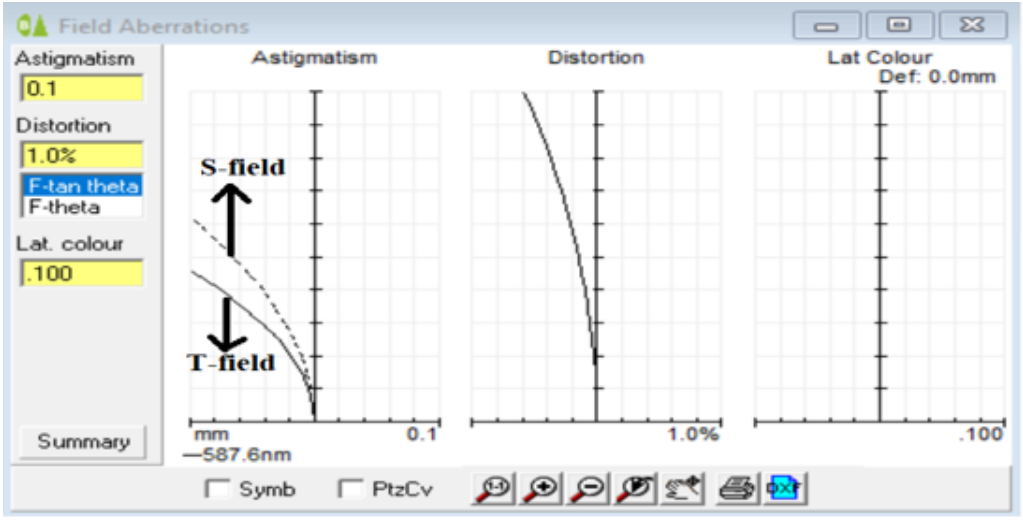

Figure 3.19: Field aberrations of achromat lens for a focal length of 8 mm.

When we compare the spot diagrams for the chromatic case from Figures 3.14 and 3.18, the points are more focused to the center for the achromat lens compared to the bi-convex lens, where it was more spread out. This proves that chromatic aberration for different wavelengths is reduced significantly with achromat lens in comparison to bi-convex lens. The astigmatism, Figure 3.15 compared to 3.19, is similar for both lenses, which still has to be corrected and is explained in the later stages of this chapter. In conclusion, the usage of an achromat lenslet offers significant advantages over a bi-convex single lens without increasing the system complexity. This is due to the inherent correction of the chromatic aberrations, improved imaging performance, increased design flexibility, and the availability of achromat lenses with standard focal lengths at only moderate cost difference to spherical lenses. These advantages make achromats also a preferred choice in many optical applications that demand high-quality, color-corrected imaging and precision.

3.3.2 Simulation using curved image surface

Field curvature is an optical aberration that occurs when an optical system, such as a lens, does not produce a flat image plane for objects located at different distances from the lens. In the context of WinLens, field curvature is an important parameter that describes the shape of the image field formed by a lens system. Field curvature in WinLens is often described in terms of the radius of curvature. If the radius of curvature is positive, the image field is curved outward; if it is negative, the field is curved inward. The extent of curvature in the visual field is described by the radius of curvature's magnitude. As our main focus is to minimise astigmatism, which is dependent on S and T-field, Field curvature is a compromise for both and is explained visually on the right side in the Figures 3.20 and 3.21: The circle of least confusion (CLC) which lies in between the T- and S- field aberration curves is compensated by the pos. and neg. values in case of the curved image plane.

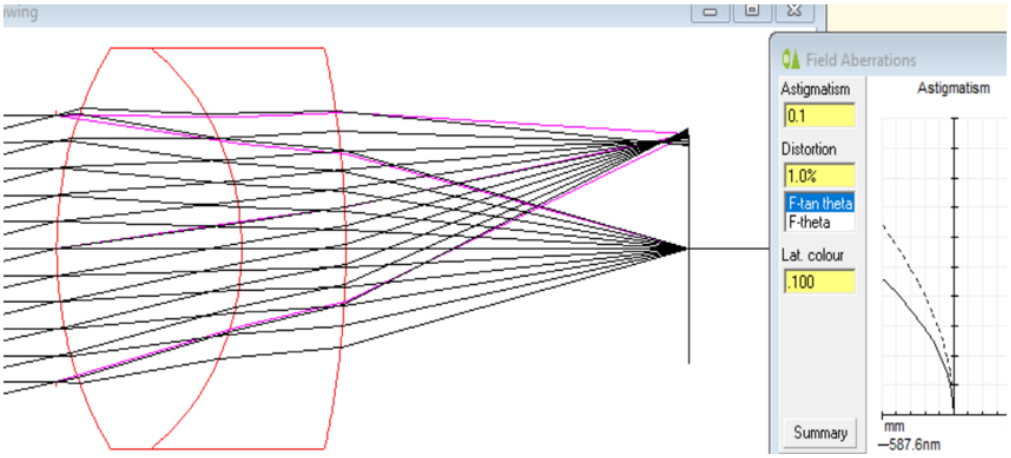

Figure 3.20: Astigmatism showing S and T-field for plane image plane.

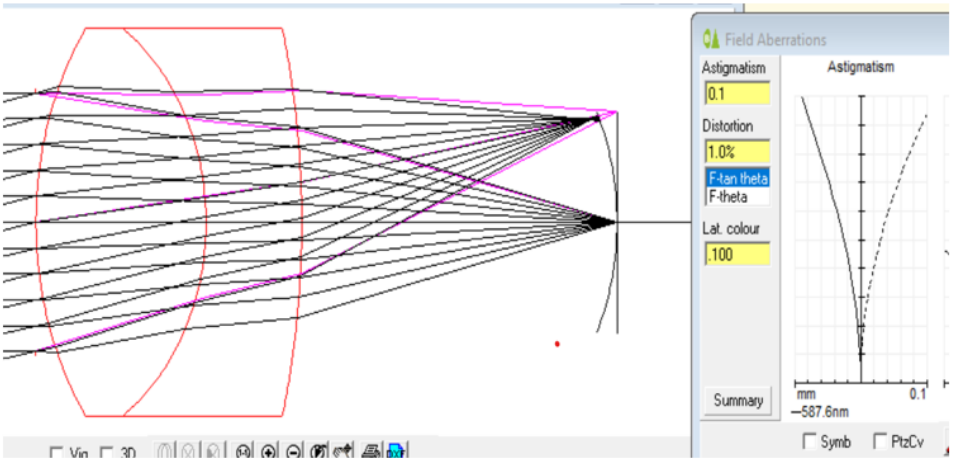

Figure 3.21: Astigmatism showing S and T-field for curved image plane.

3.3.3 Image sharpness and radius of field curvature

An essential aspect of optical simulation is image sharpness, which has a direct impact on the final image's clarity and quality. As shown in the previous section the remaining field curvature of the lens is a major variable that affect how sharp an image will be. With our premise of using an achromat lenslet for low system complexity the remaining radius of the field curvature can be determined in optical simulation so that the bending of the image sensor can be altered accordingly. By manipulating the bending radius to the lens' field of curvature, we can

control the way light rays converge or diverge on the pixel array, ultimately influencing the focus and clarity of the image formed.

We will have a deeper look into the calculation of the radius of curvature obtained from WinLens data for the lens' field curvature for plane objects. This will be combined with theoretical calculations based on the lens equation for curved objects with a significant expansion in Z direction since this further influences the image projection and focusing on the pixel array.

Cylindrical Curved object

WinLens is primarily used for designing and analyzing optical systems, including lenses, but it does not have the capability to simulate curved objects. The ray tracing, spot and astigmatism diagrams that are shown in the previous section are all simulated using a flat object. The objective for this thesis is also to find the bending radius or the radius of curvature for a curved object. Since this was not possible using WinLens, we decided to do it in a hybrid approach by numerically combining simulation data for flat objects from WinLens with results obtained by the lens equation for curved objects. For this thesis, we have used a cylindrical object such as a Coca Cola can of radius 30 mm, used e.g. for print quality inspection. To do this, I had to come up with a sketch for a curved object and do respective measurements with different angles and calculate measurements such as object distance, image distance, object height and image height. Before that Figure 3.22 gives an overview on geometry and symbols used for the lens equation 3.1, magnification 3.2 and half-sided viewing angle 3.3 complying with WinLens' coordinates (Z, Z', Y, Y') where f is the focal length of the lens and m the magnification of the projection. As mentioned earlier in section 3.1.2, the object distance has negative values related to the Z-coordinate axis.

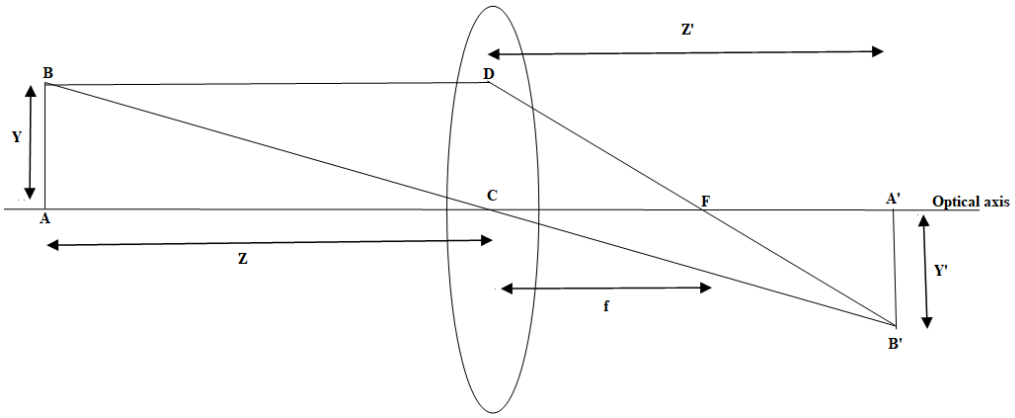

Figure 3.22: Lens equation Geometry.

Lens equation,

$$\frac{1}{f} = \frac{1}{-Z} + \frac{1}{Z'} \tag{3.1}$$

Magnification,

$$m = \frac{Y'}{Y} = \frac{Z'}{Z} \tag{3.2}$$

Half-sided viewing angle,

$$\omega = \arctan(\frac{Y}{Z}) = \arctan(\frac{Y'}{Z'}) \tag{3.3}$$

With a half object height of Y = 30 mm at a distance of Z = -150 mm and a focal length f = 8 mm of the achromat lens the image height Y', distance Z' and the half-sided viewing angle can be calculated using lens equation (or with the PreDesigner software accompanying WinLens, Figure E.1 in the appendix). The image height is around 1.7 mm at a distance of 8.45 mm as shown in Table 3.1.

Table 3.1: Design parameter for the Achromat lens and the Coca Cola can based on lens equation

Parameters	**Values**
Focal length f	8 mm
Object Distance Z	-150 mm
Image Distance Z'	8.45 mm
Object height Y	30 mm
Object angle ω	-11.31 deg
Image height Y'	-1.69 mm

With this the symmetrical double-sided image height (2Y') is around 3.4 mm which fits within the longer side of the imager's pixel area in full resolution of around 3.5 mm from image specifications Table 2.1. Therefore, it is proven that in order to project the full object diameter of the beverage can within the longer side of the pixel area the lens with 8 mm focal length in WinLens and the existing achromat lens with 7.5 mm focal length for practical measurements, introduced in section 2.4.2, can be used.

Image surface of cylindrically curved object

The sketch in Figure 3.23 gives the geometric overview on calculations for cylindrically curved objects, like the beverage can. Coordinates of object points (Z, Y) on the cylinder surface facing towards the lens are described by radius r_0 and angle α around the center distance z_0 on the optical axis as given in equation 3.2 and 3.3 with α = -90° – +90° (half-sided 0 – +90°).

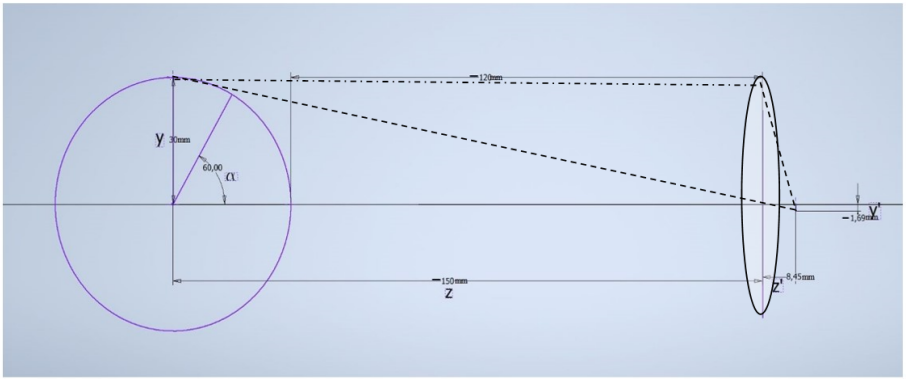

Figure 3.23: Geometric sketch for a curved object.

Coordinates of the projected image points (Z', Y') by an ideal lens are calculated on basis of the lens equation solved for Z', equation 3.6 and 3.7. Equivalent to the image height Y', the field fraction FF normalized to Y'_{max} can be given by eq. 3.8, when results have to be further combined with coordinates simulated in WinLens.

Object distance,

$$Z = z_0 + r_0 \cos \alpha \tag{3.4}$$

Object height,

$$Y = r_0 . \sin \alpha \tag{3.5}$$

Image Distance,

$$Z' = \frac{(f * Z)}{(f + Z)} \tag{3.6}$$

Image height,

$$Y' = Y * \frac{Z'}{Z} \tag{3.7}$$

Field Fraction,

$$FF = \frac{Y'}{Y'_{max}} = \frac{Y}{Y'_{max}} * \frac{Z'}{Z} \tag{3.8}$$

Calculating the projected image points (Z', Y') in this way with the design parameter corresponding to Table 3.1 with z_0 = 150 mm, r_0 = 30 mm, Y'_{max} = -1.69 mm and for the angle range α = -90° – +90° results in symmetrical plot of image surface for the cylindrical curved object for the ideal lens in Figure 3.24.

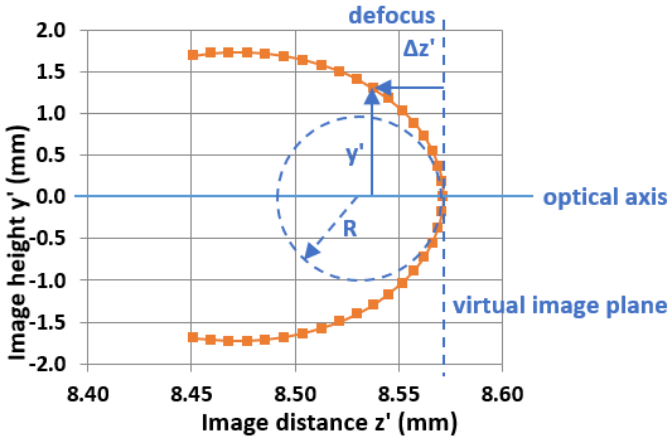

Figure 3.24: Image surface of the cylindrical curved object for the ideal lens.

Normally only the defocus ΔZ' as a function of image height Y' is of interest, which is the difference against a virtual image plane as defined in Figure 3.24 above. This symmetrical defocus function ΔZ' = ΔZ'(Y') is plotted in Figure 3.25 below for the half-sided image height. E.g. at image height Y' = 1.0 mm the defocus equals ΔZ'= 0.019 mm. With this diagram representation ΔZ' = ΔZ'(Y') further defocus contributions from lens aberrations obtained from WinLens for real lenses can be added up. Also, the radius of curvature of the osculating circle R at the origin can be extracted by means of a polynomial trend-line as an estimate of the necessary bending of the imager foil.

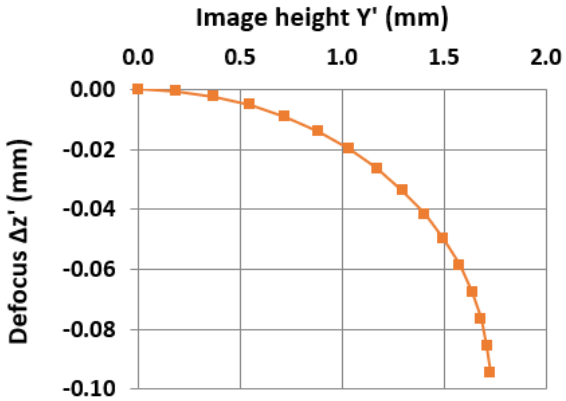

Figure 3.25: Defocus ΔZ' as a function of image height Y' of the cylindrical curved object for the ideal lens.

3.3.4 Exporting WinLens simulation results

Now, we consider WinLens simulation results for an additional defocus due to field aberration of real lenses which are obtained for flat objects. Astigmatism in conjunction with the Petzval Field curvature, Figure 3.10, is the main contribution and data can be exported from WinLens' graphical interface in Figure 3.19 into an Excel-sheet. It is as a set of values retrieved from ray tracing of 20 object points (in the plane at Z = -150 mm) uniformly spread over the normalized field fraction from 0 (optical axis) to 1 (at |Y'max|= 1.69 mm) in steps of 0.05. The relevant data we use are the field fraction (for calculating the image height) and the field curve giving the defocus for the circle of least confusion CLC (which is the mathematical average of tangential and sagittal surfaces at a given image height).
The Excel calculation sheet in Table 3.2 shows the **Field Fraction** steps and respective **Field curve** deviations exported from WinLens in the first and fourth column, respectively. In the second column the **Image Height** is calculated using equation 3.8 and in the third column the defocus values **Delta z' from lens eq.** of Figure 3.23 for the cylindrical curved object are interpolated for the uniform field fraction steps. In the last column named **Lens eq + field curve** both defocus values are added up for each step.

Table 3.2: Data from WinLens and imported to Excel for calculation.

Winlens			Field curve (winlens)	Field curve and Lens eq.
FieldFrac	Image Height(mm)	Delta z' from lens eq	Fieldcurve(mm)	Lens eq+ Field Curve
0.00	0.00	0.000	0.0000	0.0000
0.05	0.08	0.000	-0.0009	-0.0012
0.10	0.17	-0.001	-0.0035	-0.0040
0.15	0.25	-0.001	-0.0078	-0.0090
0.20	0.34	-0.002	-0.0139	-0.0159
0.25	0.42	-0.003	-0.0217	-0.0248
0.30	0.51	-0.004	-0.0312	-0.0357
0.35	0.59	-0.006	-0.0424	-0.0485
0.40	0.68	-0.008	-0.0552	-0.0633
0.45	0.76	-0.010	-0.0697	-0.0800
0.50	0.85	-0.013	-0.0859	-0.0987
0.55	0.93	-0.016	-0.1036	-0.1194
0.60	1.01	-0.019	-0.1229	-0.1419
0.65	1.10	-0.023	-0.1437	-0.1666
0.70	1.18	-0.027	-0.1661	-0.1931
0.75	1.27	-0.032	-0.1899	-0.2219
0.80	1.35	-0.038	-0.2151	-0.2528
0.85	1.44	-0.044	-0.2418	-0.2862
0.90	1.52	-0.052	-0.2698	-0.3223
0.95	1.61	-0.063	-0.2991	-0.3621
1.00	1.69	-0.079	-0.3297	-0.4087

3.3.5 Discussion of the simulation results

Three data columns from Table 3.2 namely Delta z' from lens eq. (col.3), Field curve (col.4) and Lens eq + field curve (col.5) are plotted over the Image Height (col.2) in Figure **??** showing the different the different defocus contributions:

- **Delta z' from lens eq.** is the deviation in the image plane for the curved object assuming an ideal lens with no aberration. At the max image height of 1.69 mm (last row of Table 3.2)it is 24% of the lens aberration given by the **Field curve**.
- **Field curve** gives the image curve deviations for field curvature of a flat object obtained for the 8 mm achromat lens simulated from WinLens. This deviation is the desired bending surface for a plain object.
- **Lens eq + field curve** is the overall deviation which is the sum of the deviation from curved object (column 3 in Table 3.2) and the deviation from the flat object of WinLens (column 4 in Table 3.2). This overall deviation is the desired bending surface for the curved object.

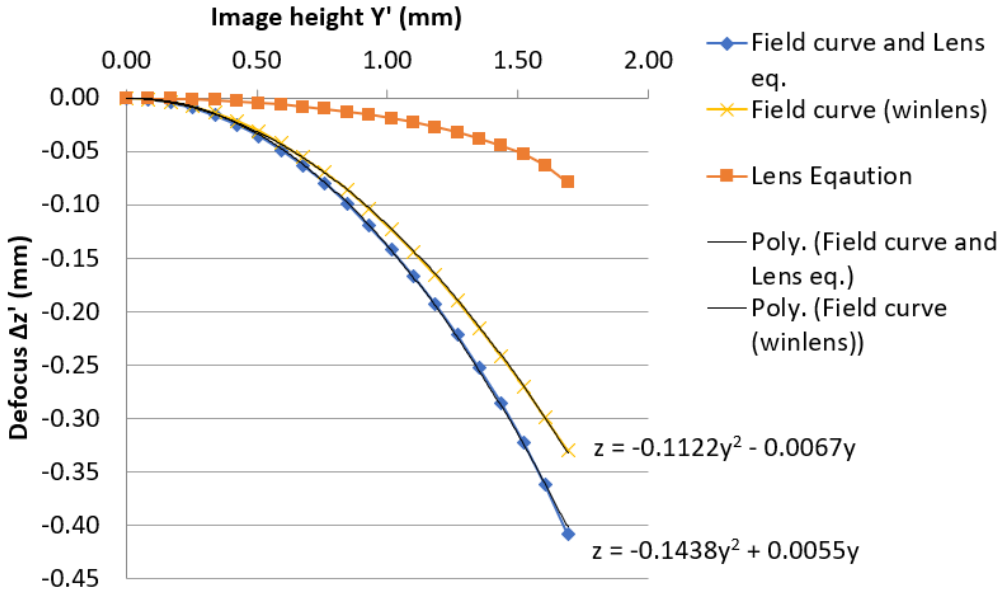

Figure 3.26: Graphical observation of the defocus contributions and curvature of the image surfaces.

From the two curves, **Field curve** and **Lens eq + field curve**, we obtained the respective polynomial equations using the trendline option in Excel. Using the second order coefficient of these trendlines from the curves, we can calculate the radius of curvature using the methodology given below.
The radius of curvature R of the osculating circle of the function z= z(y) is defined by,

$$R = \frac{(1 + (\frac{dz}{dy})^2)^{\frac{3}{2}}}{\frac{d^2z}{dy^2}} \tag{3.9}$$

For the symmetric trend-line of 2. Order, we can neglect the first order coefficient, therefore

$$\frac{dz}{dy} = 2a_2 * y \tag{3.10}$$

where a_2 is second order coefficient.

$$\frac{d^2z}{dy^2} = 2a_2 \tag{3.11}$$

At the origin on the optical axis for y=0 and $\frac{dz}{dy} = 0$, equation 3.9 becomes,

$$R = \frac{1}{2a_2} \tag{3.12}$$

Where $\frac{dz}{dy}$ and $\frac{d^2z}{dy^2}$ are the first and second derivatives of the equations from the curves. Using these equations from the graph in Figure 3.26 and the equation for Radius of curvature R in 3.12 we found the bending radius of -4.45 mm for the flat object curve of WinLens (Field curve only) and -3.47 mm for the curved object (field curve and the lens equation). This way we can theoretically calculate the required radius of curvature for the image plane around the optical axis (Y' = 0) and use it as an estimate for the mechanical mount of the CFP imager foil. In the next section, we will see the implementation of this using different lenses and a hardware setup.

3.4 Summary

In this section, we learned about WinLens, along with some of its features and the coordinate system it uses. We also discovered the various lens options as well as the various forms of aberrations. Then, using WinLens, we compared these lenses' simulations. Additionally, we then found out about image sharpness and calculation of radius of curvature for curved objects.

4 Optical system construction

4.1 Embedding foil on a bendable material

Embedding a foil on a bendable material can be done using various methods, depending on the specific requirements and materials involved. Firstly, selection of the material is very important. We have used a bendable metal sheet and can embed an aluminum foil or, in this case a polymer foil. Next, the bendable material was cleaned to ensured it was free from grease, dust or any other contaminants that may affect the adhesion. In the next step, for adhesive selection, we have used soft gum to embed the foil on the bendable metal sheet and spread it over with a brush and ensured it did not affect the flexibility of the foil.

The positioning of the foil on the bendable metal was a big challenge as we had to position the center of the image sensor on the center of the bendable metal so that the optical axis was observed at the center of the field of view on the image. Although, since this was done manually and accounted for human errors, this positioning was not so accurate. We will have a deeper insight on this in the later stage of this chapter. The embedding of the foil is shown in Figure 4.1. Once the foil was glued onto the bendable material, it was pressed and secured, and then allowed to cure. Now the bendable foil was ready to be used. In the next section, we will explore the mechanical setup and construction of the optical system.

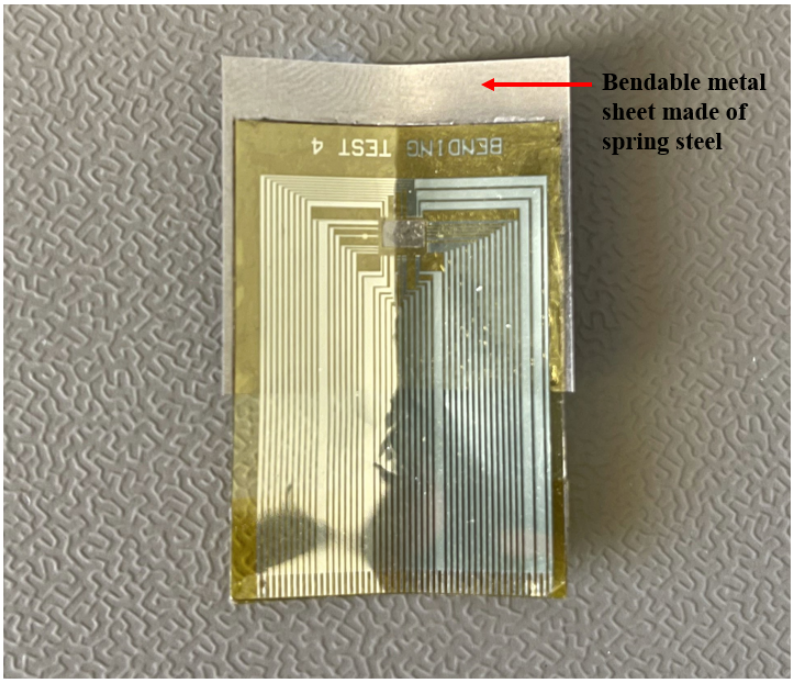

Figure 4.1: Embedded foil on a metal sheet.

4.2 Mechanical setup of the optical system

The mechanical setup of an optical system is a critical aspect that directly impacts the system´s performance, stability, and reliability. It involves the careful design, construction, and arrangement of mechanical components and structures to support and align the optical elements in the desired configuration. A well-engineered mechanical setup ensures precise positioning, stability, and efficient transmission of light, enabling the optical system to achieve optimal functionality and meet specific performance requirements.

One important aspect of the mechanical setup is the selection and design of mechanical components and structures, such as optical mounts, stages, rails, and brackets. The choice of materials is crucial to ensure rigidity, stability, and compatibility with the optical elements and the surrounding environment. Mechanical components should be fabricated with high precision to minimize any mechanical distortions or misalignments.

Alignment and positioning mechanisms are another essential element of

the mechanical setup. These mechanisms allow for precise adjustment and alignment of the optical elements, including lenses, mirrors, filters, and beam splitters. Micrometer screws, fine-tuning stages, and kinematic mounts are commonly used to achieve accurate positioning and alignment. The mechanical setup should provide ease of adjustment, repeatability, and stability to ensure precise alignment of the optical components for the desired optical performance.

The mechanical setup should also consider ease of maintenance and accessibility. Optical systems may require periodic adjustment, cleaning, or component replacement. Therefore, the mechanical design should facilitate convenient access to critical components and allow for easy disassembly and reassembly without compromising the alignment or stability of the system. In this thesis, we have built a similar mechanical setup using optical elements such as lenses, stages and mounts to achieve the desired optical performance. A micrometer screw was used to move the lens towards the image sensor while it was subject to bending, thereby increasing the object distance accordingly for better clarity of the image. The same is represented in Figure 4.2.

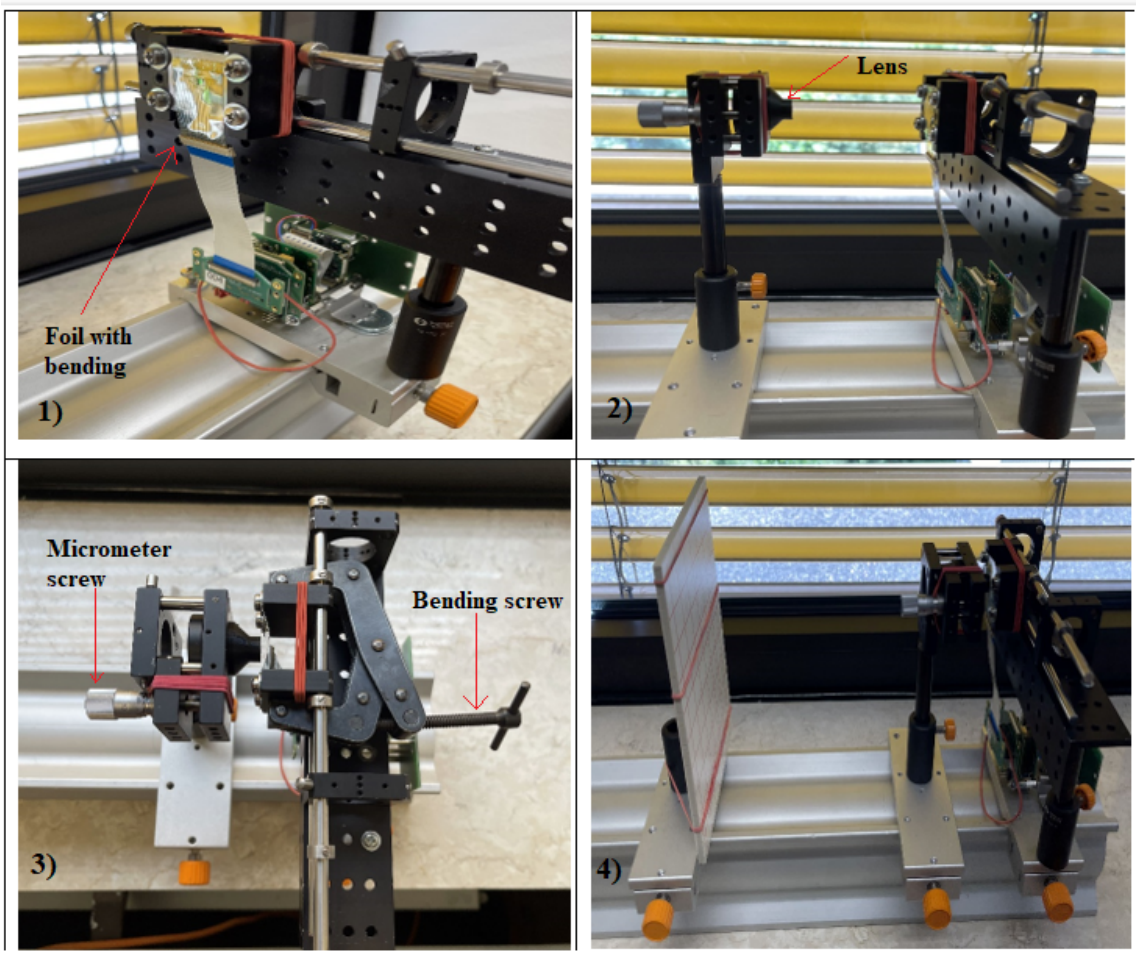

Figure 4.2: Mechanical arrangement of optical system. 1) Bending Foil 2) Lens 3) Bending apparatus 4) Plane object test setup.

The positioning and alignment of the lens and image sensor on the foil was a tedious process. To verify if the foil was embedded on the metal sheet correctly, meaning to check if the image sensor was placed at the center of the metal sheet, we conducted a mechanical check to determine if the optical axis was at the center of the field of view. Figures 4.3 and 4.4 provide an explanation of this process.

In Figure 4.3 1), we can observe the manual verification using a scale to check if the alignment is on a straight line. In Figure 4.3 2), the LED is focused on the image sensor, but not exactly at the center of the image sensor. This discrepancy occurred due to human error during the

process of attaching the foil onto the metal sheet. Figure 4.4 confirms that the center of the image sensor or the optical axis is not located at the center of field of view.

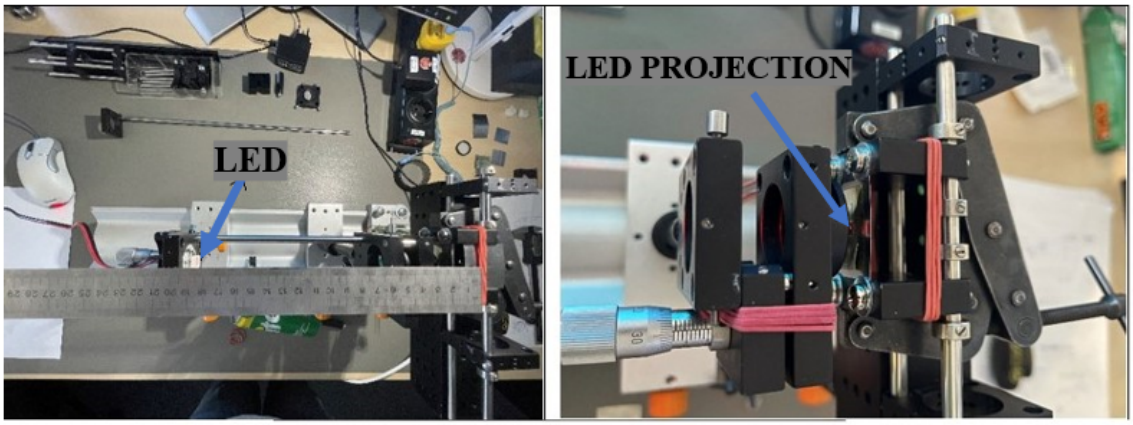

Figure 4.3: Optical axis verification: Checking alignment using the scale (Left). The LED is focused on the image sensor (Right).

We used a micrometer screw in attachment with the lens to address the defocusing issue caused by bending the foil. By adjusting the micrometer screw, we were able to move the lens towards the sensor, allowing us to observe and measure the defocus in millimeters.

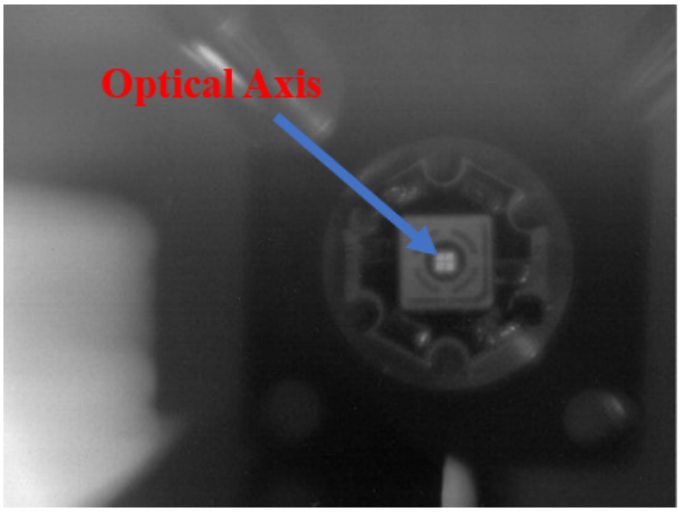

Figure 4.4: Image of the projected LED on the image sensor taken with the readout electronics. The optical axis is marked by the luminated LED center.

The setup for the foil attached to the PCB was screwed to the base to prevent any mechanical movement that could potentially damage the foil during bending. The PCB received data from the foil, which was then displayed on the software through the computer connected via LAN. In this mechanical setup, we utilized objects such as Coca Cola can to observe curved object. This can be particularly useful in applications where quality assurance is important, as it allows us to check the smoothness of the curvature. We have used it also because of its cylindrical shape which enable us to make similar curvature in WinLens software. Additionally, we used a siemens star printed on a plane sheet for the plane image observation. The resolution of optical equipment, is tested using a Siemens star. On a white background, it consists of a pattern of white "spokes" that radiate from a central point and get wider as they move out from it. The spokes and the spaces between them get smaller the closer to the center one looks, but they never touch except at the exact center of the star [32], see Figure 4.5.

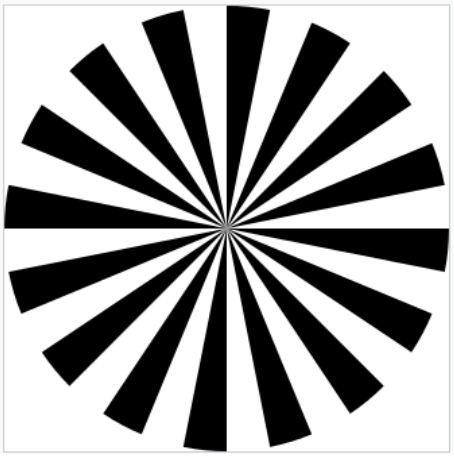

Figure 4.5: Siemens Star. Source: [32].

The block diagram of the entire measurement setup is shown in Figure 4.6. The final mechanical setup of the optical system is shown in Figure 4.7. In the next section we will delve into image observation, calculation, and verification of the radius of curvature.

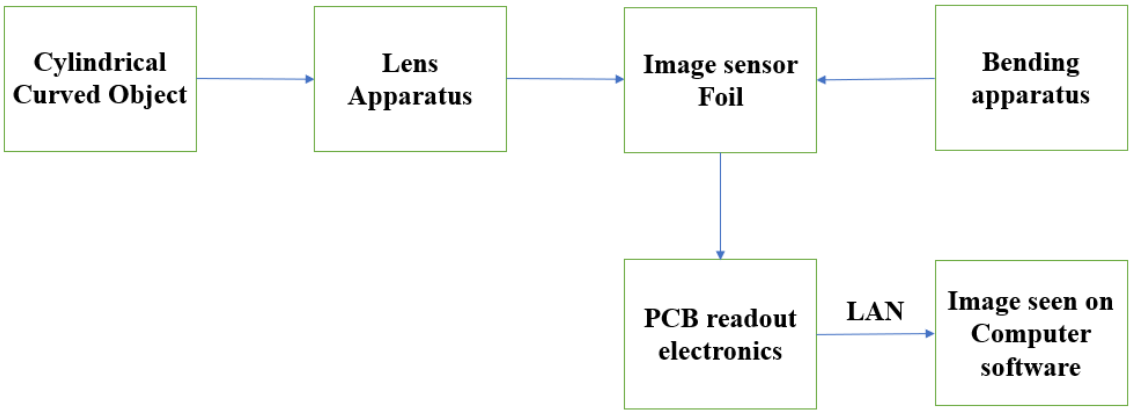

Figure 4.6: System block diagram including Optical, mechanical and electrical parts.

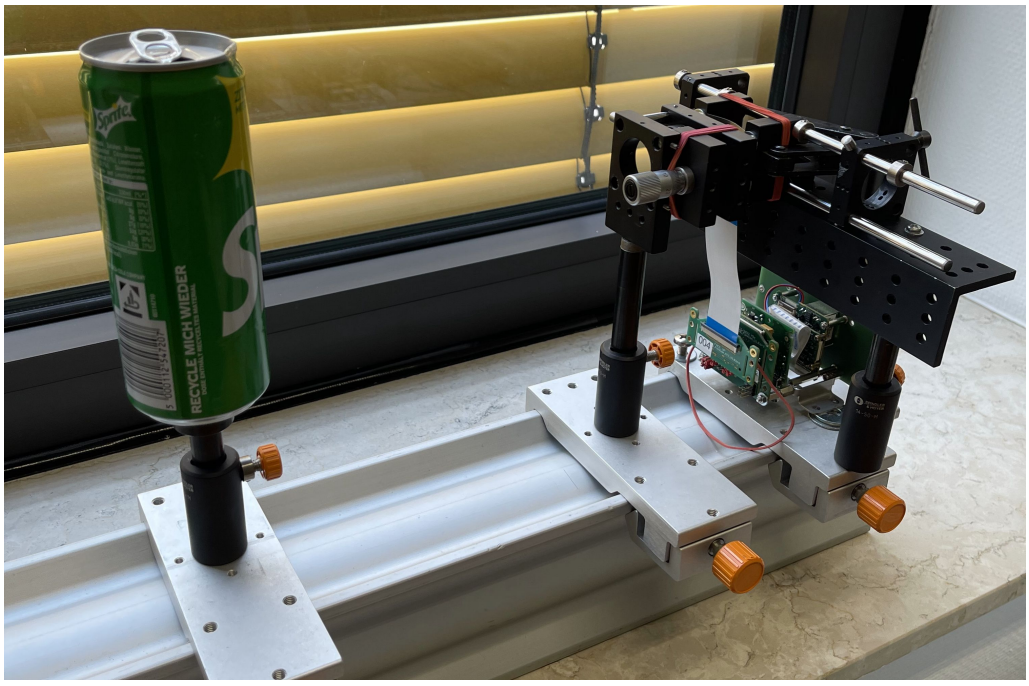

Figure 4.7: Final Measurement setup of the optical system.

4.3 Measurement Results

4.3.1 Radius of curvature

Image observation is a fundamental process and one of the key aspects of image observation is the quality of the acquired images. The clarity and resolution of the images significantly impact the observer's ability to extract accurate and valuable information.
In our thesis, as mentioned earlier, we simulated the objects for different lenses including biconvex and achromat lenses. Using these simulation data, we observed images obtained with these lenses. However, due to the lower accuracy of the biconvex lens, we decided to proceed with achromat lenses with different focal lengths. In the upcoming section, we will examine how the images appear when the image sensor is plane and during bending.
Before diving into the image observations, we derived a relationship between the bending radius and the inner (curve) distance to calculate the bending radius. Figure 4.8 provides a schematic explanation. From the images we can observe how the vernier reading is measured for bending. V in mm is the vernier bending, D in mm is the distance of the solid structure holding the metal sheet, and d in mm is the inner (curve) distance which is calculated as d= V- 2D in mm. The objective is to find the inner distance d in relation with bending radius in mm. By knowing the vernier reading, we can calculate the bending radius.

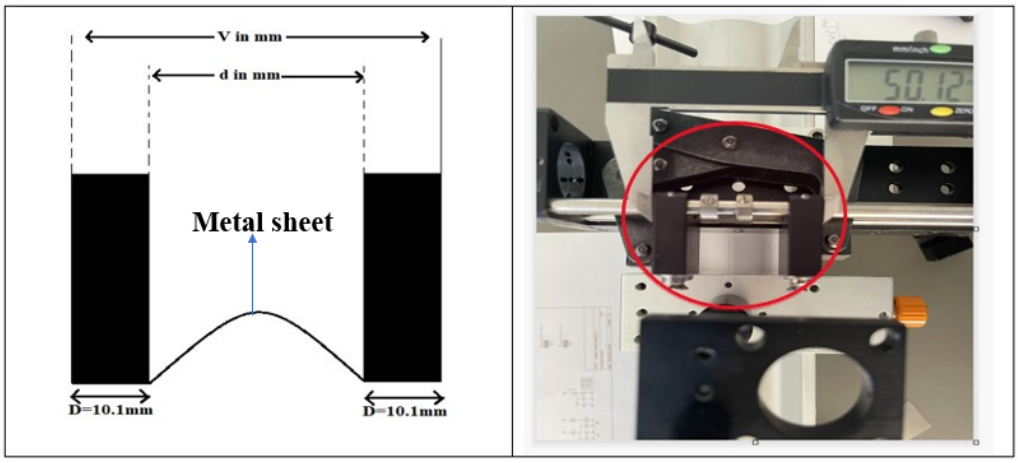

Figure 4.8: Schematic sketch of the vernier reading compared to the vernier reading in the image.

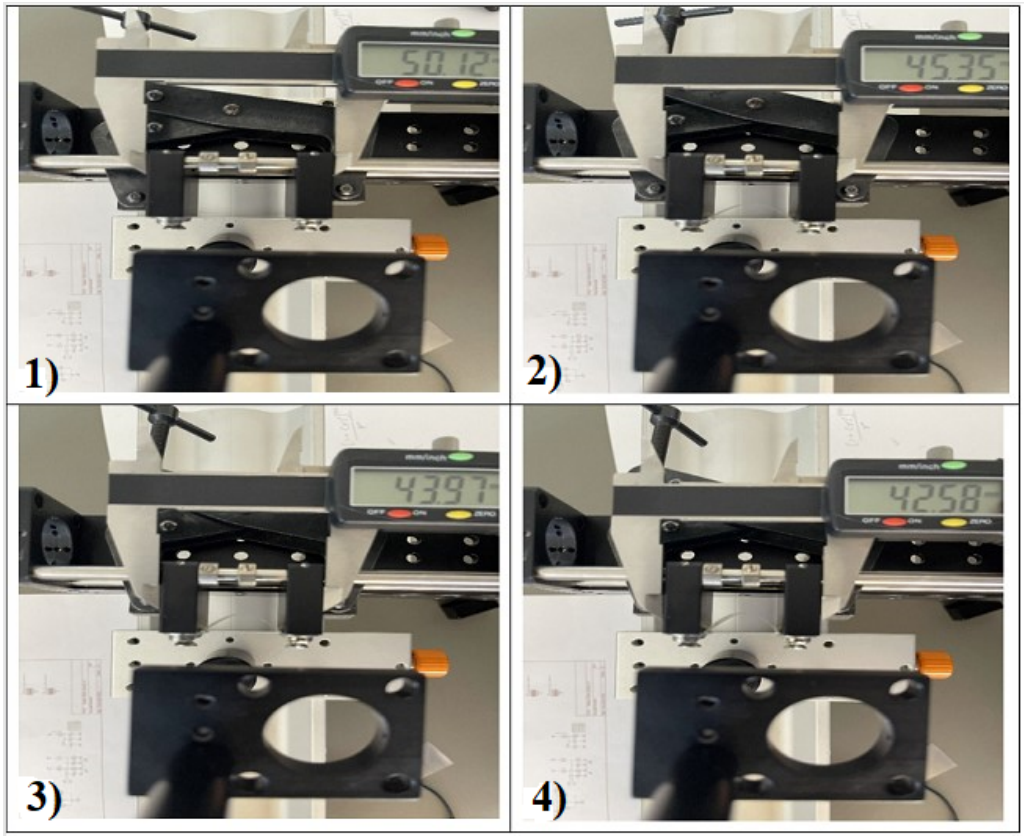

Figure 4.9: Increasing Bending of image sensor foil with respective vernier width. 1) 50.13 mm 2) 45.35 mm 3)43.97 mm 4)42.58 mm.

From Figure 4.9 we can see different bending of the foil and the respective vernier bending. Using these images and IrfanView software, we extract points (x,y pixel coordinates) along the bended metal sheet and created a dataset in an excel sheet. By using the trendline equation and the equation 3.9 mentioned in the previous chapter, we calculated the radius of curvature for each respective vernier reading. The results of these calculations can be seen in Table 4.1, and the respective graph is presented in Figure 4.10 for a vernier reading of 42.58mm. The orange highlighted box shows the symmetric center of the curve.
This was repeated for different bending curves and the respective radiuses were calculated. Since we now have the radiuses for different vernier reading, we can plot the graph between inner distance d (d= V-2D) in mm and the calculated radiuses shown in Table 4.3. This graph is shown in the Figure 4.11. From this graph, we can establish

the relationship using the trendline equation. However, it's important to note that this equation may not be entirely accurate and could be subject to an difference of approximately ± 2%. This is because for d= 28.55 mm we got a Radius of curvature of R = -11.99 mm but we should have ideally got a value of -12.20 mm.

Table 4.1: Data collected from IrfanView software and calculated to observe the same curve of bending 42.58 mm in Excel.

V in mm	42.58				
x_pix	y_pix	x in mm	y in mm	x_offset in mm	y_offset in mm
408	558	-69.77	-95.42	-9.92	-8.21
399	543	-68.23	-92.86	-8.38	-5.64
387	531	-66.18	-90.80	-6.33	-3.59
379	521	-64.81	-89.09	-4.96	-1.88
362	512	-61.90	-87.55	-2.05	-0.34
350	510	-59.85	-87.21	0.00	0.00
338	512	-57.80	-87.55	2.05	-0.34
323	521	-55.23	-89.09	4.62	-1.88
310	531	-53.01	-90.80	6.84	-3.59
299	543	-51.13	-92.86	8.72	-5.64
285	558	-48.74	-95.42	11.12	-8.21

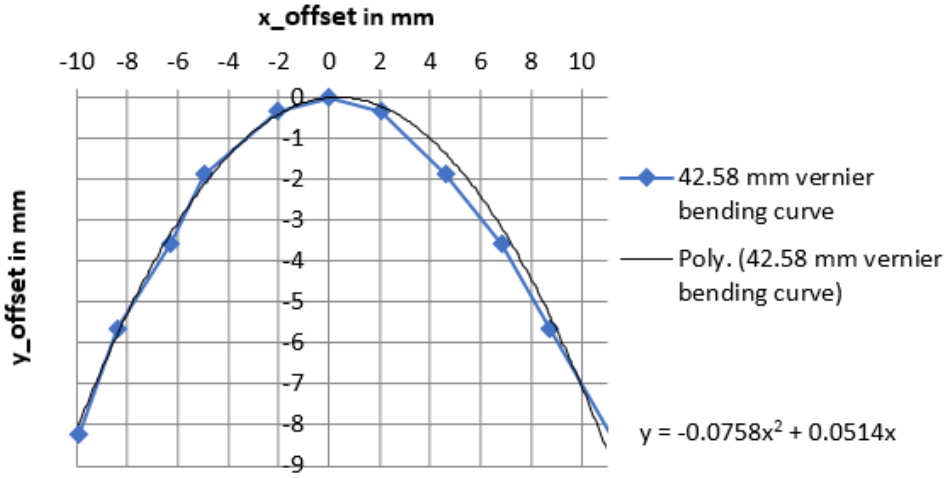

Figure 4.10: The curve for 42.58 mm bending.

Table 4.2: Data for respective for inner distance d and ROC in mm.

Distance d in mm	Radius of Curv in mm
22.38	-6.85
23.77	-8.47
25.15	-9.43
28.02	-11.36
28.55	-12.20

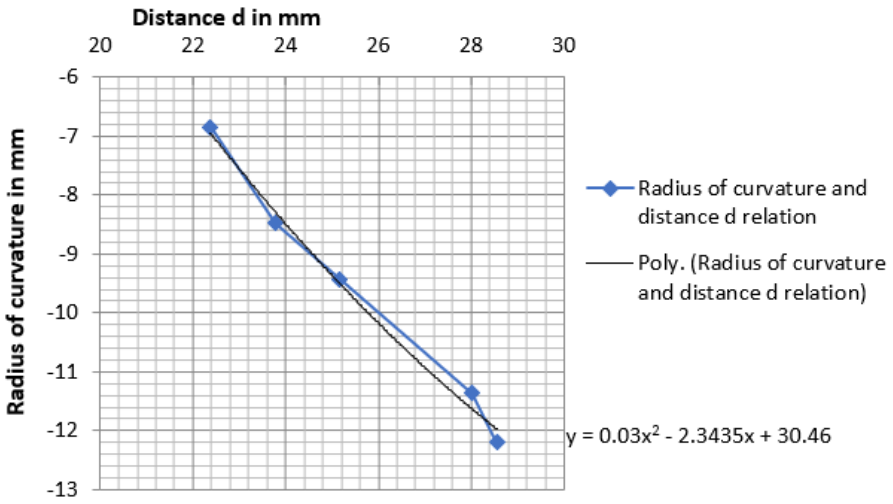

Figure 4.11: Graph and equation to calculate Radius of curvature in relation to inner distance d.

From this graph in Figure 4.11 the relation is given as,

$$R = 0.03\,d^2 - 2.3435\,d + 30.46 \tag{4.1}$$

4.3.2 Image Acquisition and Analysis

During the image observation, we used two achromat lenses with focal lengths 15 mm and 7.5 mm. The 15 mm was used for pre-testing and 7.5 mm lens for final measurements and comparison with the simulation results. We chose these lenses based on their availability in the office and their suitability for our image sensor, which was determined using the lens equation and other relevant parameters. The mechanical setup

for the different lenses was adjusted in accordance with image distance and object distance, with the aperture wide open. First let's examine the image observation using the 15 mm lens and a Coca Cola can as the object. While observing through this lens, we had recorded images at the initial position which is the plane image sensor and then respectively increasing the bend thereby decreasing the inner distance d in mm. Figure 4.12 shows the readings from plane image sensor, a bend with V= 45 mm and V= 42.5 mm.

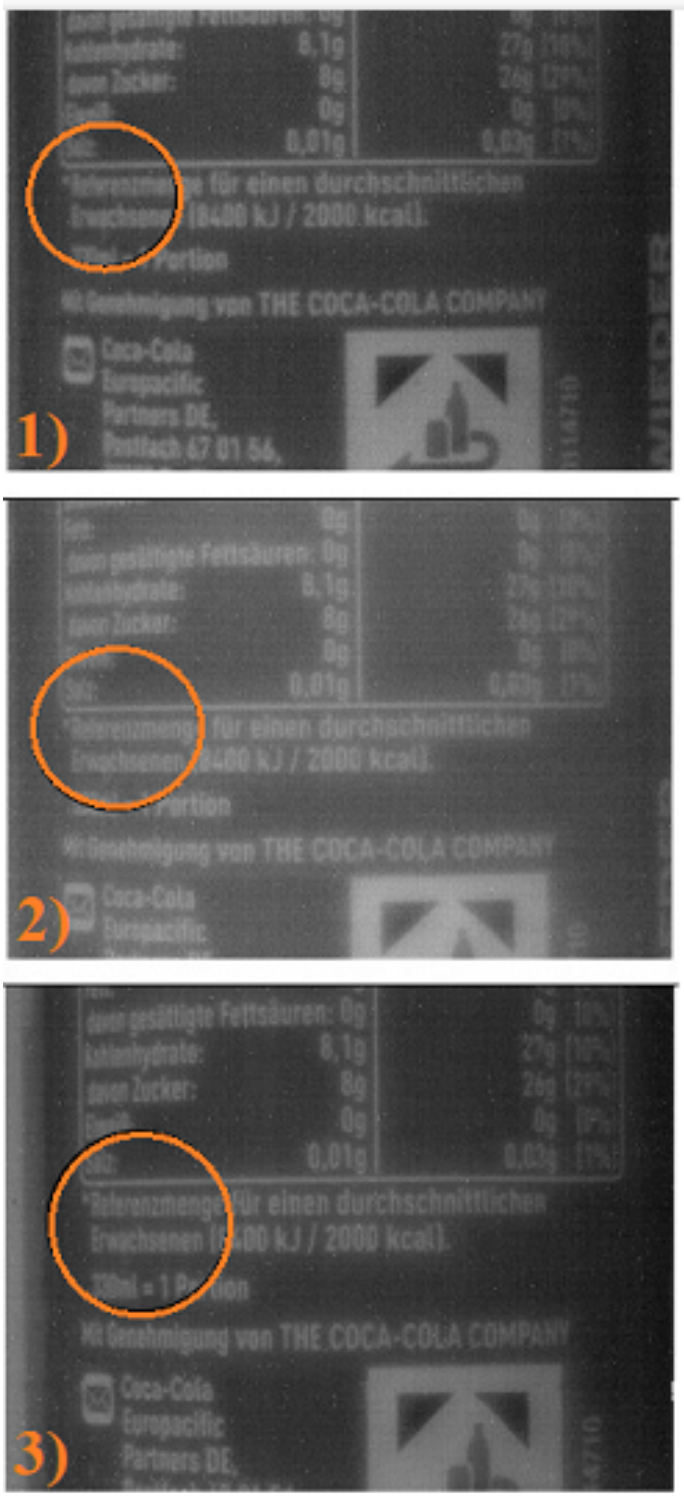

Figure 4.12: Pre-test images on the 15 mm achromat lens. 1) Plane image sensor with no bend 2) Bending with V=45 mm 3) Bending with 42.5 mm.

As we can see from the Figures 4.12, there is better clarity on the edges of the image with 42.5 mm bend than when the image sensor was plane. For this specific bending with a vernier reading of V=42.5 mm, calculate the radius of curvature using the relationship between d and R described in Equation 4.1 and it resulted in radius of curvature of -6.88 mm. Similarly, we repeated the observation using the 7.5 mm lens, with the Coca Cola can as the object. The images from the same are shown below.

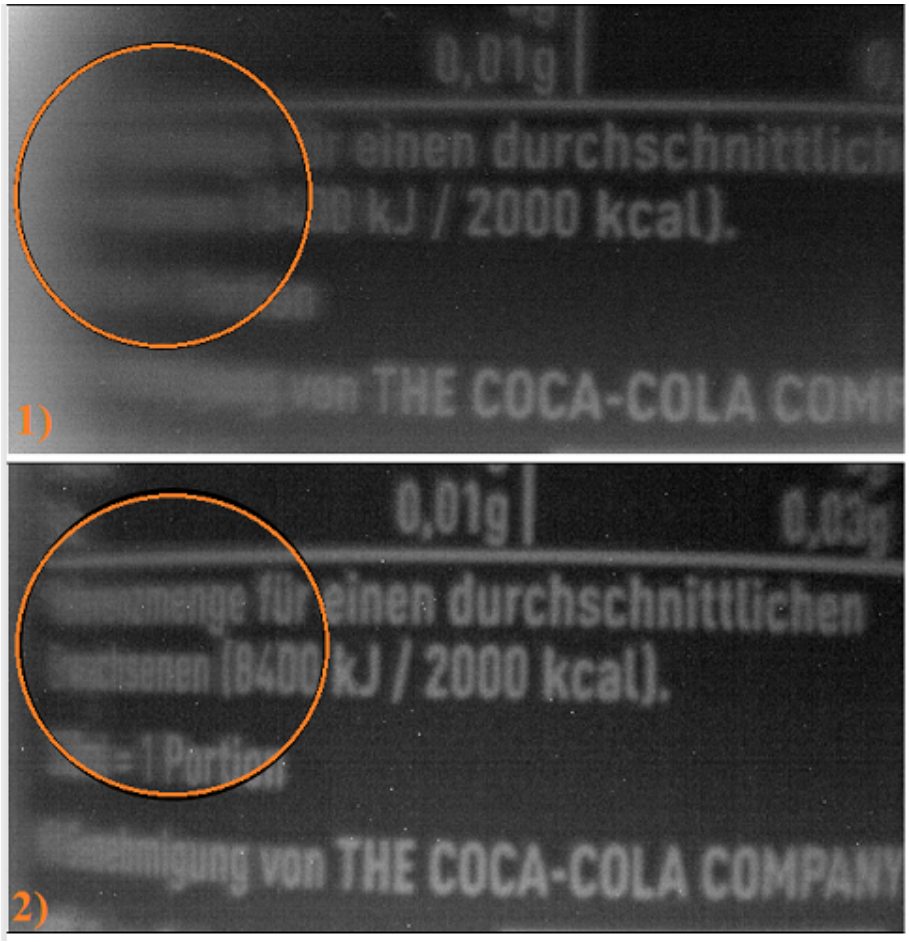

Figure 4.13: Images on the 7.5 mm achromat lens. 1) Plane image sensor with no bend 2) Image sensor with the bend of V= 40.5 mm.

From Figure 4.13, we can observe that with the bending of V= 40.5 mm, the edges of the image exhibit significantly improved clarity compared to those captured with a plane image sensor. To calculate the radius of curvature for this bending, we use the same equation (Equation 4.1) that relates the inner distance (d) to the radius of curvature (R). The calcu-

lated radius of curvature is -4.75 mm, with a difference of approximately ±2%. When compared it to the Radius of curvature in the simulation results for a curved object of -3.47 mm, the difference is +36%. This is because during the bending measurement, we bent the image sensor to a vernier distance of V = 40.5 mm and we could see the difference in the image clarity between the plane image sensor and the bent sensor very clearly. There was also a risk of the image sensor being damaged on further bending, therefore I stopped at bending of V =40.5 mm. Additionally, using the 7.5 mm achromat lens, we also tested the plane object: a Siemens star printed on a paper. The focused was set on the middle row of 3x3 Siemens star array. The image for the same is shown in Figure 4.14.

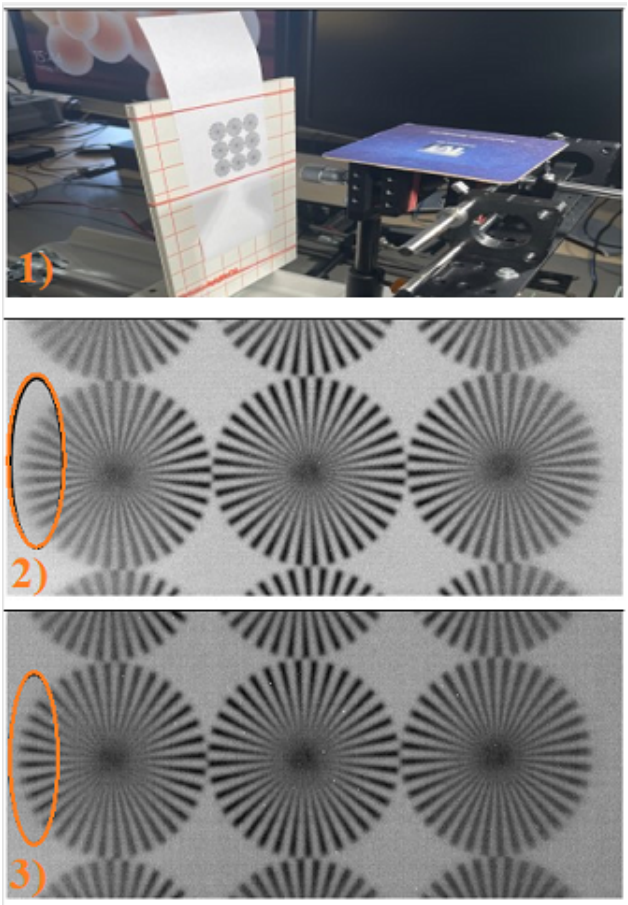

Figure 4.14: Images on the 7.5 mm achromat lens. 1) Plane object of Siemens star 2) Plane image sensor 3) Bending of V=40.5 mm.

For the bending of 40.5 mm for the plane object observation, radius of curvature R = -4.73 mm. When compared it to the radius of curvature in the simulation results for a flat object of -4.45 mm, the difference is +6%, see Table 4.3. Based on the above observations and calculations, we can infer the quality of the image and its relationship to the radius of curvature.

Table 4.3: Comparison of measurement and simulated results.

Objects	**Radius of curvature simulated**	**Radius of curvature measured**	**Deviation**
Curved (Coke can)	-3.47 mm	-4.75 mm	+36 % *
Flat (Siemens star)	-4.45 mm	-4.75 mm	+6 %

*Refer to remarks in the text.

4.4 Summary

In this section, we have explored and discussed several aspects related to the embedding of the foil on a metal sheet, as well as the measurement setup and image observation process. We discussed the challenges in positioning the foil on the metal sheet and also the importance of the mechanical setup in achieving optimal performance, stability, and reliability of the optical system. Furthermore, we presented the process of calculating the radius of curvature in relationship with the bending distances. Lastly, we did the image observation and calculated the relation of radius of curvature to the sharpness and clarity of the image and compared to the results from simulation.

5 Conclusions and Outlook

Curved image sensors have shown significant potential in improving optical performance and reducing aberrations. Despite challenges in manufacturing, ongoing efforts are expected to overcome these obstacles, driving wider adoption and integration into various imaging devices.

In this thesis, we explored the history of curved image sensors and their applications in everyday life. We also learned about the Chip Film Patch (CFP) technology, the manufacturing process, and existing approaches. The Integration of the chip system into a foil was also discussed in detail.

In the next chapters, we saw an introduction to optical simulation software, learnt about its coordinate systems, lenses it has to offer and different types of aberrations in optics. We then used different lenses to see the simulation and observe their respective field aberrations and spot diagrams and saw how the field curvature best fits. We also analysed image sharpness in WinLens for a plane object and also did a manual calculation and observation considering the curved object. By combining the resulting two image curvatures, we calculated the radius of curvature using the graphs and trendline equations.

In the next chapter, we had an insight on the hardware measurement setup of the optical system and considered different objects for observation. We conducted image analysis and compared the sharpness between a plane image senor and a gradually bent image sensor. We developed a manual method for calculating the radius of curvature of the bent image sensor on the metal sheet. We then compared these calculated values with the results obtained from simulations, finding them to be similar with an accuracy of approximately 36% for the curved object and 6% for a flat object. Therefore, the expected bending of the image sensor was observed with the measurement setup.

In conclusion, the future of curved image sensors looks promising, with potential advancements poised to transform photography, computer vision, and specialized applications. As technology progresses, we can expect a new area of imaging capabilities and experiences, where curved image sensors play a pivotal role in delivering high-quality and immersive visual content.

Bibliography

[1] W. Gao, Z. Xu, X. Han, and C. Pan, "Recent advances in curved image sensor arrays for bioinspired vision system," *Nano Today*, vol. 42, p. 101366, 2022.

[2] R. Dinyari, S.-B. Rim, K. Huang, P. B. Catrysse, and P. Peumans, "Curving monolithic silicon for nonplanar focal plane array applications," *Applied Physics Letters*, vol. 92, no. 9, p. 091114, 2008.

[3] B. Guenter, N. Joshi, R. Stoakley, A. Keefe, K. Geary, R. Freeman, J. Hundley, P. Patterson, D. Hammon, G. Herrera *et al.*, "Highly curved image sensors: a practical approach for improved optical performance," *Optics express*, vol. 25, no. 12, pp. 13 010–13 023, 2017.

[4] A. F. Abbasi *et al.*, "Curvilinear electronics and optoelectronics for healthcare," *Advanced Materials*, 2018.

[5] J. G. Park *et al.*, "Bendable and stretchable silicon image sensor." *Nature Communications*, 2014.

[6] M. S. Jeong *et al.*, "Recent progress in materials and devices toward printable and bendable organic electronics." *Journal of Materials Chemistry*, 2013.

[7] Y. Zhang *et al.*, "Bendable hybrid organic-inorganic perovskite photodetectors." *Advanced Functional Materials*, 2019.

[8] D. H. Kim, N. Lu, R. Ma, Y. S. Kim, R. H. Kim, S. Wang, and J. A. Rogers, "Epidermal electronics." *Science*, vol. 333(6044), pp. 838–843, 2011.

[9] H. Li, Y. Li, X. Li, H. Li, J. Li, and J. Li, "Hybrid electronics: an emerging technology for wearable devices," vol. 16(45), 2020.

[10] M. Stoppa and A. Chiolerio, "Hybrid electronics: a review of thin-film device-based microelectronics and its potential for implantable and wearable applications." *Journal of Applied Physics*, vol. 116(5), p. 051101., 2014.

[11] H. Ren, J. Wu, Z. Wu, W. Wang, Z. Lai, and Z. Wang, "Hybrid electronic skins for human-machine interfaces." *Advanced Materials*, vol. 33(6), p. 2003995, 2021.

[12] J. Kim and D. H. Kim, "Wearable and flexible electronics for continuous molecular monitoring." *Chemical Society Reviews*, vol. 48(7), pp. 1826–1852, 2019.

[13] A. Golzar, "Hybrid system-in-foil integration and interconnection technology based on adaptive layout technique," *Institut für Nano- und Mikroelektronische Systeme der Universität Stuttgart*, pp. 14–71, 2019.

[14] S. Wang, J. D. Schulze Spüntrup, B. Albrecht, C. Harendt, and J. N. Burghartz, "Processing and chracterisation of an ultra-thin image sensor chip in flexible foil system," *Institut für Nano- und Mikroelektronische Systeme (INES)*, 2022.

[15] X. Huang, J. Yu, and C. Xie, "Recent advances in flexible and wearable sensors for continuous health monitoring." *Chemical Engineering Journal*, vol. 353, pp. 1–15, 2018.

[16] *Technical Datasheet, VGA4 Specification*, "IMS CHIPS", May 2005, version 0.5.

[17] "Edmund optics," https://www.edmundoptics.com/p/5mm-dia-x-75mm-fl-mgfsub2sub-coated-achromatic-doublet-lens/5873/.

[18] R. Kingslake, "Lens design fundamentals." *Academic Press*, 2010.

[19] "Winlens user manual," http://www.winlens.de/.

[20] P. Smith, "Chromatic aberration correction in consumer cameras: A review." *Optics Express*, vol. 27(10), pp. 13 582–13 604, 2019.

[21] "Chromatic aberrations," https://svi.nl/Chromatic-Aberration.

[22] X. Zhang, Q. Sun, and X. Yuan, "Design of aspheric lenses for correcting spherical aberration in an optical disk pickup head." *Applied Optics*, vol. 57(13), pp. 3351–3358, 2018.

[23] "Spherical aberrations," https://i0.wp.com/digitalphotographylive.com/wp-content/uploads/2012/04/Spherical-aberration.png?ssl=1.

[24] P. H. Hansen, M. S. Grane, and S. A. Sørensen, "Coma corrector for astronomical telescopes." *Optics Express*, vol. 29(2), pp. 2457–2466, 2021.

[25] "Coma aberrations," https://www.lumenera.com/blog/six-optical-aberrations-that-could-be-impacting-your-vision-system.

[26] X. Dai, H. Zhang, and F. Yuan, "A novel method for correcting optical astigmatism using a toric lenslet array." *Optics Express*, vol. 28(4), pp. 5676–5686, 2020.

[27] "Astigmatism." [Online]. Available: https://www.edmundoptics.eu/knowledge-center/application-notes/imaging/how-aberrations-affect-machine-vision-lenses/

[28] E. Hecht and A. Zajac, *Optics*. ADDISON-WESLEY PUBLISHING COMPANY, 1987.

[29] A. Nussbaum, "Geometrical optics | aberrations," in *Encyclopedia of Modern Optics*, R. D. Guenther, Ed. Oxford: Elsevier, 2005, pp. 11–19. [Online]. Available: https://www.sciencedirect.com/science/article/pii/B0123693950006886

[30] J. Schwarz, "Distortion correction for lens-based imaging systems." *Optics Express*, vol. 25(4), pp. 4540–4552, 2017.

[31] "Distortions," https://www.eckop.com/resources/optics/aberrations/.

[32] "Siemens star," https://en.wikipedia.org/wiki/Siemens_star.

Appendices

Simulations

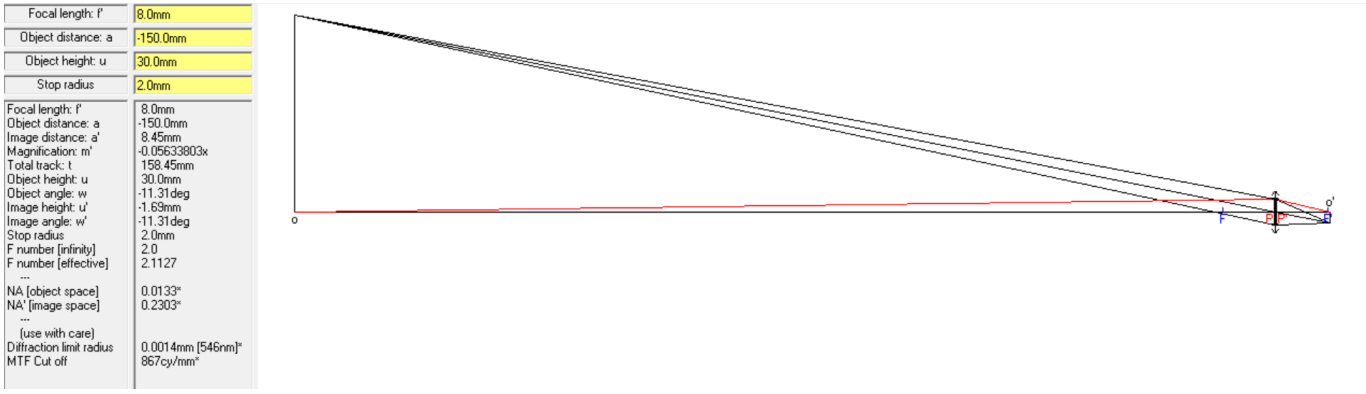

Figure E.1: Predesigner screenshot for appropriate selection of the lens

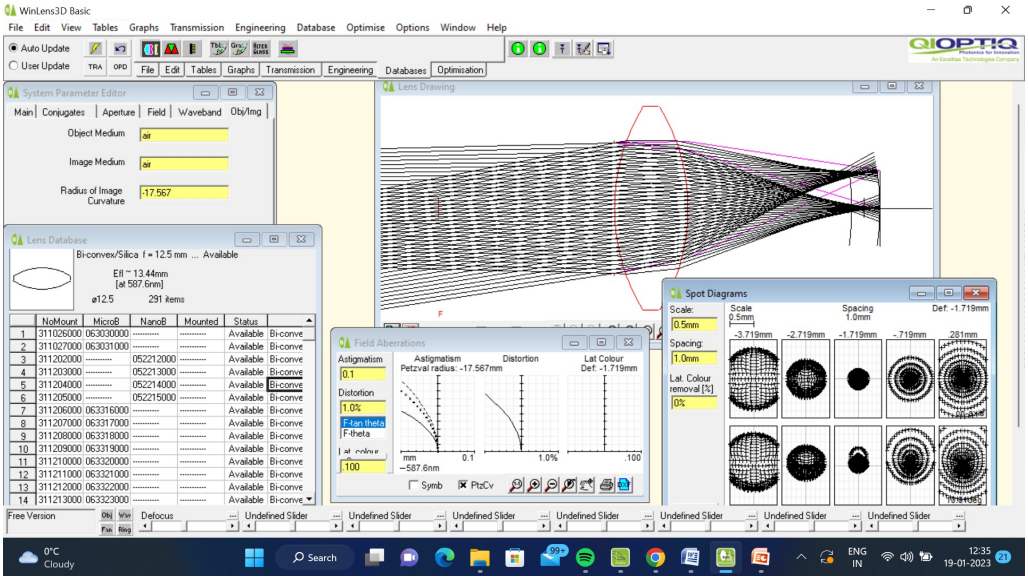

Figure E.2: Screenshot Simulation of biconvex lens for focal length of 12.5 mm

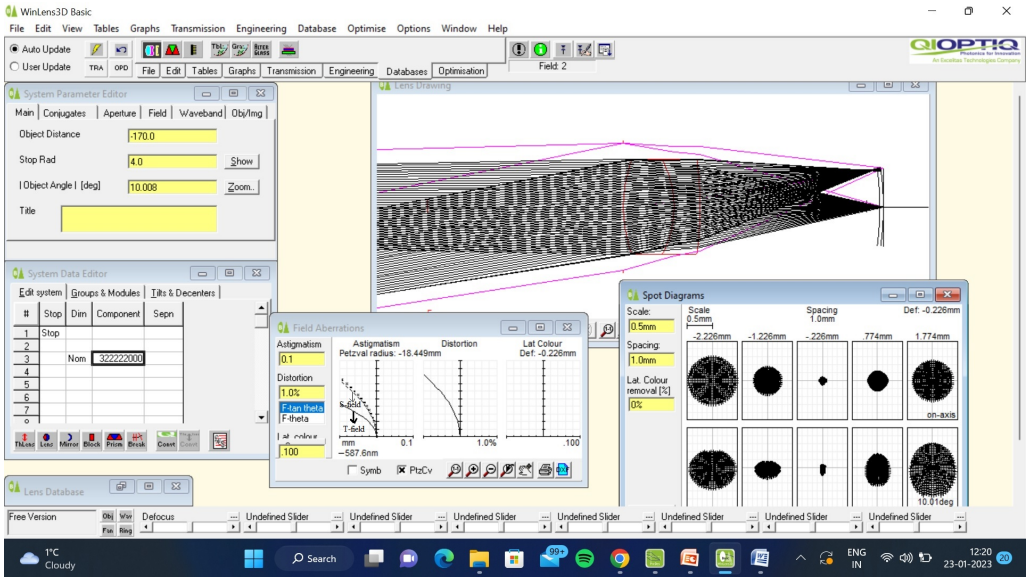

Figure E.3: Screenshot Simulation of biconvex lens for focal length of 12.99 mm

Table E.1: Calculations using lens equations for a curved object

Radius (mm)	30.000	Focal Length(mm)	8.00	Object distance(mm)	150.000	Image height(mm)	1.6900
DeltaAlpha(Deg)	5.000						
	Object			Image		Image Curvature	
Alpha(Deg)	z(Distance)	y(height)		z'(Distance)	y'(height)	FieldFrac (y'/1.69mm)	Delta z'
0	-120.000	0.000		8.571	0.000	0.000	0.0000
5	-120.114	2.615		8.571	-0.187	0.110	-0.0006
10	-120.456	5.209		8.569	-0.371	0.219	-0.0023
15	-121.022	7.765		8.566	-0.550	0.325	-0.0052
20	-121.809	10.261		8.562	-0.721	0.427	-0.0091
25	-122.811	12.679		8.557	-0.883	0.523	-0.0140
30	-124.019	15.000		8.552	-1.034	0.612	-0.0198
35	-125.425	17.207		8.545	-1.172	0.694	-0.0264
40	-127.019	19.284		8.538	-1.296	0.767	-0.0337
45	-128.787	21.213		8.530	-1.405	0.831	-0.0416
50	-130.716	22.981		8.522	-1.498	0.886	-0.0499
55	-132.793	24.575		8.513	-1.575	0.932	-0.0586
60	-135.000	25.981		8.504	-1.637	0.968	-0.0675
65	-137.321	27.189		8.495	-1.682	0.995	-0.0765
70	-139.739	28.191		8.486	-1.712	1.013	-0.0856
75	-142.235	28.978		8.477	-1.727	1.022	-0.0947
80	-144.791	29.544		8.468	-1.728	1.022	-0.1036
85	-147.385	29.886		8.459	-1.715	1.015	-0.1123
90	-150.000	30.000		8.451	-1.690	1.000	-0.1207
95	-152.615	29.886		8.443	-1.653	0.978	-0.1289
100	-155.209	29.544		8.435	-1.606	0.950	-0.1367

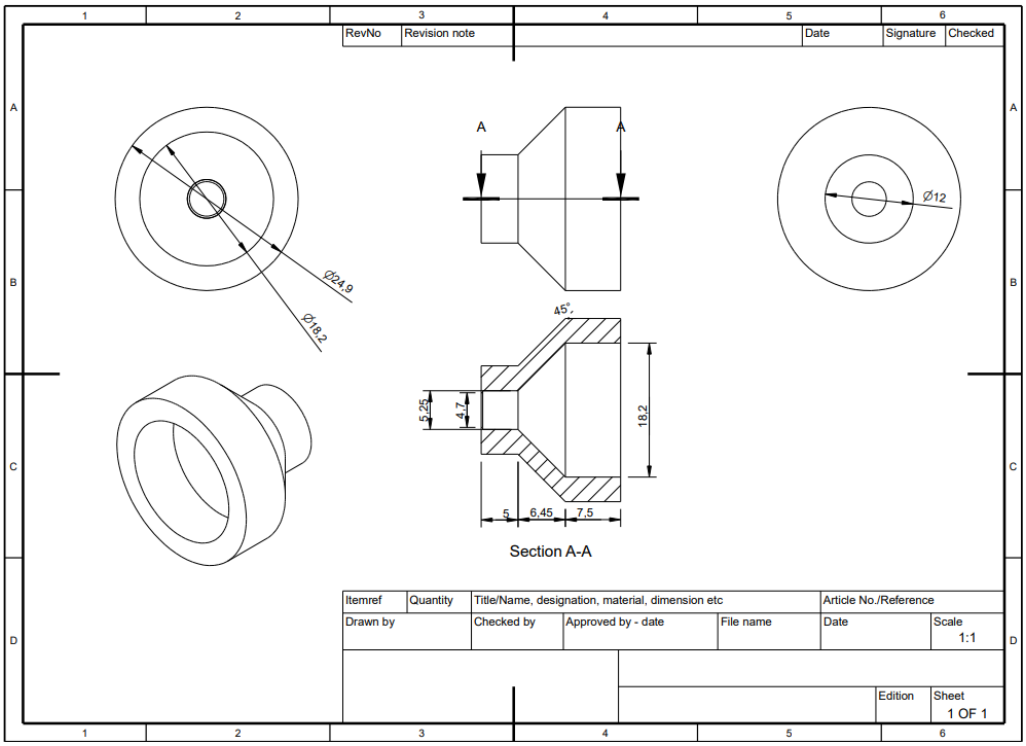

Figure E.4: Lens Holder Design.

Declaration of Authorship

I, Kevin Carlos P, hereby declare, that this thesis is my own work and effort unless stated otherwise. I certify that no other person's work has been used without proper acknowledgement. Furthermore, I declare, that this work has not been published yet and is not the object of another examination procedure.

Stuttgart, 06.07.2023